A protein-DNA surface hydrogel mechanically protects the cell nucleus

Ramesh Adakkattil[†1], Pranay Mandal[†1-3], Yahor Savich[†1-3], Valentin Ruffine[4], Mareike A. Jordan[1], Henrik Dahl Pinholt[5], Elisabeth Fischer Friedrich[4], Frank Jülicher [2,3,4*], Stephan W Grill[*1,3,4], Alexander von Appen[*1,4]

Abstract

The nuclear envelope protects the genome from mechanical stress during processes such as migration, division, and compression [1–6], but how it buffers forces at the scale of DNA remains unclear. Here, we utilize optical tweezers to show that a multivalent protein–DNA co-condensate containing the nuclear envelope protein LEM2 [7,8] and the DNA-binding protein BAF [9,10] shield DNA beyond its melting point at 65 pN. Under load, their collective assembly induces an unconventional DNA stiffening effect that provides mechanical reinforcement, dependent on the intrinsically disordered region (IDR) of LEM2. Within cells, these components form an elastic surface hydrogel at the nuclear periphery, visible as a continuous surface by cryo-electron tomography. Disruption of this surface hydrogel increases DNA damage and micronuclei formation during nuclear deformation. Together, this work expands the functional repertoire of condensates, revealing a load-responsive nuclear surface hydrogel at the mesoscale that mitigates mechanical stress.

---

[1]Max Planck Institute of Molecular Cell Biology and Genetics; Pfotenhauerstraße 108, 01307 Dresden, Germany.

[2]Max Planck Institute for the Physics of Complex Systems; Dresden 01187, Germany.

[3]Center for Systems Biology Dresden; 01062 Dresden, Germany.

[4]Cluster of Excellence Physics of Life, Technische Universität Dresden; 01062 Dresden, Germany.

[5]Institute for Medical Engineering and Science, Massachusetts Institute of Technology; Cambridge, MA, USA.

*Corresponding authors. Email: julicher@pks.mpg.de (F.J.); grill@mpi-cbg.de (S.W.G.); vonappen@mpi-cbg.de (A.v.A)

[†]These authors contributed equally to this work.

Main Text

Mechanical stress can lead to DNA damage, such as double-strand breaks or micronucleation (Extended Data Fig. 1a), both of which are associated with aging-related diseases including cancer, cardiomyopathies, and neurodegeneration [11–17]. The nuclear envelope is a mechanical scaffold that safeguards the genome [5], but how it protects the genome from mechanical stress-induced DNA damage is not well understood. The nuclear envelope is formed by a highly cross-linked network primarily composed of polymeric lamins, the outer and inner nuclear membranes (INM), and proteins that link the membrane to the encapsulated DNA [5]. Here, we focus our attention on BAF-LEM2, both essential for nuclear envelope reassembly and genome stability [6–9], that directly connects chromatin to the inner nuclear membrane [18–24]. Notably, LEM proteins such as LEM2, along with other inner nuclear membrane proteins, contain substantial intrinsically disordered regions (IDRs) that protrude into the nucleoplasm, accounting for an estimated 30% of the total protein mass at the inner nuclear membrane (Fig. 1a, Extended Data Fig. 1b, Supplementary Table 1). Proteins with extended IDRs can undergo phase separation to form biomolecular condensates [25,26] and even hydrogels [27,28]. LEM2 undergoes phase separation to orchestrate nuclear membrane assembly during mitosis, driven by its amino-terminal IDR ($LEM2_{NTD}$)[7]. Recent evidence suggests that protein-DNA co-condensation can generate forces that contribute to biomolecular organization [29–31]. Hence, we here set out to investigate potential protective functions of an extended IDR meshwork built by phase separating proteins at the nuclear surface.

Protective DNA-protein co-condensation

We first set out to rebuild the BAF-LEM2 module on DNA, and investigate its mechanical properties by use of optical tweezers. We established a minimal reconstitution system from purified components (full-length BAF and the N-terminal domain of LEM2 containing the IDR but lacking the transmembrane domain; Fig. 1a, Extended Data Fig. 1c-f) and tested if bulk phase separation can be observed, consistent with previous observation[7] (Extended Data Fig. 1k). We found that phase separated LEM2 droplets enrich BAF and DNA *in vitro* (Fig. 1b, Extended Data Fig. 1g). Since DNA, BAF and LEM2 enrich at the nuclear periphery in cells (Fig. 1c, Extended Data Fig. 1 h-j), it is possible that liquid-liquid phase separation and protein-DNA co-condensation contributes to the organization of the nuclear periphery.

We next set out to understand how BAF and LEM2 interact with individual DNA polymers. To this end, we added fluorescently labelled BAF and LEM2 to individual molecules of DNA stretched in the optical tweezer (methods, Extended Data Fig. 2a,b) and followed the association of both proteins to DNA (Fig. 1d, Extended Data Fig. 2d,

Movie S1-S2). We find that BAF homogeneously coats DNA in an apparently sequence-independent manner [32]. While we did not observe binding for LEM2 alone (500 nM; Fig. 1d, Movie S3), DNA-BAF caused instant LEM2 recruitment into a homogenous film. We conclude that, as expected[7], BAF recruits LEM2 to DNA at physiologically relevant concentrations.

Given that LEM2 can undergo phase separation in bulk[7], we next set out to investigate if BAF-LEM2 can co-condense together with DNA[30]. We first focused on BAF alone, and used the optical tweezer to stretch a single molecule of λ-DNA to 16.7 μm end-to-end-distance (corresponding to ~40 pN of DNA tension, methods). We next allowed BAF to bind, and then gradually reduced DNA end-to-end distance. In all cases we observed that DNA tension reduces in the process, but plateaus at an average of 3.3±0.8 pN (Fig. 1e, Extended Data Fig. 2f,g, methods) despite further reduction of the end-to-end distance. The occurrence of a constant tension plateau is indicative of a collective phase transition towards DNA-BAF co-condensate formation, similar to a 'sticky polymer' undergoing a globular collapse[30] (Fig. 1f, Extended Data Fig. 2e, Movie S4). We measured the associated bulk condensation energy to be 0.2±0.1 k_BT/bp (methods, Fig. 1g, Extended Data Fig. 2j,k,n). Adding 500nM LEM2, significantly below the saturation concentration[33] of LEM2 for bulk phase separation (4.0 μM, Extended Data Fig. 1k,l), results in co-condensate formation at significantly increased plateau tension and with significantly increased bulk condensation energy (4.9±0.6 pN and 0.4±.02 k_BT/bp, respectively; Fig. 1e-g, Extended Data Fig. 2h, Extended Data Fig. 2l-n, methods, Movie S5). Instead, adding a variant of LEM2 that is unable to undergo bulk phase separation but still binds BAF ($LEM2_{MUT}$, Extended Data Fig. 1f) results in only a marginal increase of both plateau tension and bulk condensation energy (4.1±0.5 pN and 0.3±.02 k_BT/bp, respectively; Fig. 1e,g). Taken together, DNA cross-bridging by BAF dimers alone can result in protein-DNA co-condensation. LEM2 stabilizes the DNA-BAF interaction, with a significant increase of the per basepair bulk co-condensation energy to a value that is ~20% of typical DNA basepair stacking energies[34]. We conclude that BAF-LEM2 can co-condense together with DNA.

Given that the bulk co-condensation energy is significant, one might expect DNA-BAF-LEM2 co-condensates to be stable and protect DNA from force-induced damage. To evaluate this possibility, we set out to unravel the co-condensates by force while investigating DNA integrity. We first focused on BAF alone. After forming a DNA-BAF co-condensate as described above, we gradually increased the end-to-end distance of DNA and recorded the tension applied (Fig. 1h, i; methods). In all cases we observed that DNA tension increases in the process, to an average disassembly tension of 34±9 pN as the co-condensate unravels through many consecutive 'ripping events', each releasing extended amounts of DNA (Fig. 1h; methods, disassembly tension is

independent of pulling speeds for speeds between 250 nm/s and 10 nm/s, Extended Data Fig. 3a). We note that co-condensate disassembly tension is higher than the tension that needs to be applied to mechanically evict nucleosomes from DNA [35,36], indicative of strong DNA-BAF interactions. Concurrently, we measured the associated co-condensate disassembly work to be 2.3±0.7 k_BT/bp (Fig. 1k). Notably, the disassembly work of DNA-BAF-LEM2$_{MUT}$ co-condensates is not significantly increased as compared to DNA-BAF co-condensates (2.6±0.6 k_BT/bp, Extended Data Fig. 3e,f). However, adding the phase-separating variant of LEM2 results in significantly increased DNA-BAF-LEM2 co-condensate disassembly tension and disassembly work (47±8 pN and 3.9±0.8 k_BT/bp, respectively; Fig. 1i, k), as well as a less pronounced 'rip pattern' (Fig. 1h). Remarkably, in all experiments involving BAF-LEM2, tension during unraveling surpasses the critical tension of 65 pN required to melt DNA. Hence, we find that 66±22% of the DNA remains localized within the co-condensate when the melting tension of 65 pN [37] is crossed for the first time, compared to 8±13% for DNA-BAF co-condensates (Fig 1j). We conclude that, generally, disassembly tension during co-condensate unraveling is more than ~10x larger than plateau tension during co-condensate formation, and the per-base pair disassembly work is ~10x larger than the per-base pair bulk condensation energy (see Fig. 1e,g,i,k). Such hysteresis arises when systems are unable to equilibrate on the experimental timescale (Extended Data Fig. 3b-d; methods) particularly when kinetic barriers during formation and dissolution are different, and is often seen in systems that undergo a mesoscale phase transition[38]. Taken together, BAF-LEM2-DNA co-condensates are stable structures that can retain DNA when subjected to external forces larger than those required to melt DNA.

Is the DNA inside these co-condensates mechanically protected? We hypothesize that cross-bridges and multivalent interactions formed by the IDR's of LEM2 proteins function to redistribute mechanical tension, effectively lowering the tension that is experienced by DNA (Fig. 1n). To test if DNA tension inside DNA-BAF-LEM2 co-condensate is lower than DNA tension outside, we applied the tension-sensitive intercalating DNA dye Sytox Orange (SO, methods)[39]. We find that at high external tension (52 pN), the intensity of SO is significantly higher outside the co-condensates (Fig. 1l, Extended Data Fig. 3g,h methods) than inside, consistent with DNA experiencing lower tension inside co-condensates as compared to outside. Furthermore, addition of the single-stranded DNA (ssDNA) sensor, FUS (Extended Data Fig. 3i-k)[30,40], reveals that at tensions up to ~85pN, DNA only melts outside the co-condensate and not inside (Fig. 1m, methods, Movie S6). We conclude that external tensions that are applied to DNA-BAF-LEM2 co-condensates likely percolate and redistribute throughout the object, leading to an overall reduction of DNA tension inside. Therefore, protein-DNA co-condensates formed with multivalent protein-protein interactions can protect DNA from force-induced melting.

A reinforcing response

Multiple studies have reported that when cell nuclei are mechanically deformed and undergo nuclear blebbing, rupture, or micronucleation, BAF and LEM2 rapidly associate to DNA that is mechanically stressed, exposed, or even expelled to the cytoplasm, likely to revert the damage[9,11,22,23,41,42]. We therefore wondered if the *de-novo* assembly process of the BAF-LEM2 module on naked, mechanically stressed DNA imparts a more active role in protecting DNA. To mimic such a re-assembly scenario under mechanical stress, we again stretched a single molecule of λ-DNA to 16.7 μm end-to-end-distance (corresponding to ~40 pN of DNA tension), but now monitored changes in DNA tension (by a value ΔT) during module assembly in a constant trap position protocol (methods). Notably, we observed that in the first 100 seconds after addition of BAF-LEM2, the beads in both optical traps are pulled inwards, due to a pulling tension generated by the module assembly process that opposes the external tension applied by the two traps (Fig. 2a). This resulted in a DNA tension increase by ΔT = 7.5±0.9 pN, despite the high initial DNA tension of 40 pN (Fig. 2b, methods). We note that neither the addition of BAF alone, nor adding BAF together with the $LEM2_{MUT}$ resulted in a significant tension increase (Fig. 2b, ΔT = -0.2±0.9 pN for BAF; ΔT = 1.8±0.7 pN for BAF-$LEM2_{MUT}$). Finally, we find that ΔT increases with increasing LEM2 concentration, and that, remarkably, ΔT increases in an apparently linear fashion with initial DNA tension (Fig. 2c). The module thus displays features of a reinforcing response: the higher the mechanical load on DNA, the more this module pulls back while re-assembling.

We next set out to shed light on the mechanism that underlies this reinforcing response. The linear dependence of tension increase ΔT on initial tension suggests that LEM2 and its IDR interactions introduce an additional compliant element. We therefore set out to determine the compliant properties (i.e. effective stiffness and rest length, Extended Data Fig. 4a) of the combined DNA-BAF-LEM2 module in comparison to naked DNA alone. We applied an initial tension between 20 and 40 pN, added BAF and LEM2, and then gradually increased extension while recording tension to measure the effective stiffness of the entire assembly (Fig. 2d, Extended Data Fig. 4b). We find a linear relationship in the regime between 20 - 45 pN, with an effective stiffness ~1.3±0.1 fold higher than for naked DNA (assuming saturation, K_0+K_i = 67±3 pN/μm; compared to K_0 = 51±2 pN/μm, Fig. 2d). Notably, the effective stiffness increases in a saturating manner with increasing LEM2 concentration (Fig. 2e, Extended Data Fig. 4f). We obtained an effective rest length by extrapolating the linear fit to vanishing tension (Fig. 2d, Extended Data Fig. 4b,c; methods), and found no significant difference between the two conditions (15.84±0.02 μm without BAF-LEM2 module, compared to 15.84±.01 μm with BAF-LEM2 module). Together, these results suggest a picture where LEM2 IDR-IDR interactions generate compliant elements of identical rest length assembled in parallel

to DNA (Fig. 2f). We capture this mechanism in a theoretical description that considers DNA mechanics in the enthalpic regime together with module assembly energetics (stiffening reinforcement model, SI): DNA is described as a chain of spring elements, and the assembly of BAF-LEM2 modules results in the inclusion of additional spring element in parallel and without a rest length change (SI, methods, Extended Data Fig. 4c-f). This description accounts for the dependence of stiffness on concentration (Fig. 2e, Extended Data Fig. 4e,f) as well as the measured dependencies of ΔT on initial tension and LEM2 concentration. We note that assembling compliant elements in parallel generates a reinforcing response, as can be seen in Fig. 2d when keeping the end-to-end distance fixed: the higher the initial tension, the higher the tension increase upon module assembly (red arrows).

A nuclear surface hydrogel

We next set out to explore how assembling BAF-LEM2 on the chromatin surface, with its reinforcing properties arising through the formation of IDR-dependent compliant elements, impacts nuclear integrity and morphology (Extended Data Fig. 5a). We first investigated the architecture of the chromatin surface at high resolution. We examined three independent tomograms of ion-beam-thinned sections targeting the chromatin surface, imaged using cryo-electron tomography (Fig. 3a, Extended Data Fig. 5b,c) [43]. AI-guided segmentation revealed the nuclear periphery as a continuous, largely amorphous-appearing layer with an average thickness of 14 nm between the inner nuclear membrane and nucleosome-organized chromatin (Extended Data Fig. 5e). In line with previous reports [44,45], this amorphous layer includes the filamentous lamins (Extended Data Fig. 5d) as well as the membrane-bound LEM2 molecules on a BAF cross-linked chromatin layer [9]. From these observations we suggest that the nuclear periphery is a multicomponent surface hydrogel crosslinked with the help of BAF[46–48], and linked to the membrane via LEM2 and other LEM molecules.

We next set out to investigate how material properties of this surface hydrogel are modulated when BAF is removed and the BAF-LEM module is inactivated. We first evaluated our ability to reduce BAF levels in the cell, using confocal imaging coupled with segmentation of the nuclear surface in endogenously tagged BAF-mNeonGreen HCT-116 cells (Extended Data Fig. 7a-e). We find that the nuclear periphery typically contains $(3.6\pm0.8)*10^5$ BAF dimers, reduced by 90% to $(3.6\pm0.8)*10^4$ dimers under BAF RNAi (Table 1, Extended Data Fig. 5f-h, see methods). We next set out to measure the effective area modulus of the nuclear surface hydrogel using AFM indentation experiments coupled with confocal imaging (Fig. 3b, Extended Data Fig. 8a,b). We used the AFM cantilever tip to indent the nuclei of latrunculin A-treated cells (methods). To estimate the effective area elastic modulus, we performed measurements of the mechanical work required to increase the nuclear surface area, which was determined

through confocal imaging (Fig. 3b, Extended Data Fig. 8c). We find that the effective area elastic modulus of the nuclear surface hydrogel is decreased by 36 ± 4% in BAF depleted cells as compared to control cells (from 1.8±0.2 pN/nm to 1.2±0.1 pN/nm, Fig. 3c,d, Extended Data Fig. 8d-f; methods). We anticipate that changes in the material properties of the nuclear surface lead to corresponding changes in nuclear shape. We therefore quantified nuclear surface area and shape in control and BAF-depleted cells (Extended Data Fig. 7f-m). We find that nuclear surface area (A) is increased by 8±2% in BAF depleted cells as compared to control cells (from 516±6 μm^2 to 559±9 μm^2; Fig. 3e, Extended Data Fig. 7m; methods). We characterized nuclear asphericity defined as $(A-A_V)/A_V$, where A_V is the area of a sphere with a volume identical to that of the nucleus (SI). We find that nuclear asphericity is increased by 41±7% in BAF depleted cells as compared to control cells (from 0.070±0.002 to 0.099±0.004, Fig. 3g, Extended Data Fig. 7j; methods). We conclude that removal of BAF leads to a softening of the nuclear surface hydrogel, associated with a shape change of the nucleus towards higher asphericity and larger surface area.

We next set out to reveal how the mechanical properties of the BAF-LEM module characterized at the molecular scale with optical tweezers relate to the material properties of the surface hydrogel at the cellular scale. To this end, we put forward a mechanical description of the surface hydrogel and its dependence on BAF-LEM (Fig. 3f). We consider the surface hydrogel as a two-dimensional elastic surface enclosing the nucleoplasm of constant volume. We consider a bending modulus (κ) and a bare area elastic modulus in absence of the BAF-LEM module (λ), and capture the effect of the BAF-LEM module by introducing a surface density of additional elastic spring elements (SI, Eq. S20). The bare area elastic modulus λ is largely determined by the lamin network, and the elastic springs have the reinforcing properties described above (SI, Eq. S37). The effect of an increase of nuclear asphericity upon BAF reduction (Fig. 3g) can be accounted for if the elastic spring elements associated with the BAF-LEM module contract the surface hydrogel relative to its relaxed state due to a rest-length mismatch between the two systems, introducing a pre-stress. When BAF levels are reduced, the elastic spring elements are removed and the surface hydrogel can relax, increasing its surface area and leading to more aspherical shapes (Extended Data Fig. 6c). We next used the AFM measurements (Fig. 3e, Extended Data Fig. 8d,f) as well as the reinforcing properties of the BAF-LEM module characterized in the optical tweezer to quantitatively account for the observed nuclear shape changes upon BAF depletion, using this REst-length Mismatched Multicomponent (REMM) surface hydrogel model (SI). We use the rest length mismatch, the relaxed surface area as well as the bare area elastic modulus λ as parameters. Our analysis suggests that λ is ~25 times smaller than the effective area elastic moduli measured with the AFM in control cells. This suggests a soft lamin network providing mainly entropic elasticity [49]. Because the lamin

network is soft, changing the stiffness of reinforcing BAF-LEM spring elements has a significant effect on the material properties of the REMM surface hydrogel. This model can therefore account for the observed changes in area elastic modulus and nuclear shape. We conclude that the REMM surface hydrogel model, taking into account a stiffening effect based on LEM2 IDR-IDR interactions characterized on the molecular scale, can account for nuclear surface properties at the cellular scale.

We next asked if the IDR component of this surface hydrogel imparts specific protective functions. We find that under compression, cells depleted of LEM2 by RNAi accumulate significantly higher levels of DNA double-strand breaks (Fig. 4a,c, Extended Data Fig. 9) and display a larger degree of micronucleation (Fig 4b,d, Extended Data Fig. 10). We conclude that, consistent with our optical tweezer results and our expectations from theory, the IDR gel component, via LEM2, provides a specific protective function against mechanically induced damage.

Discussion

Here, we have used optical tweezers and *in vitro* reconstitution to show that BAF and LEM2 form multivalent protein–DNA co-condensates. We reveal that i) these multivalent assemblies shield DNA beyond its melting threshold at 65 pN of tension, and ii) their assembly on DNA stretched close to melting, generates forces that counteract the stretch. Notably, a surface hydrogel model incorporating the second effect quantitatively recapitulates elastic properties of the nuclear envelope at the cellular scale. In cells, this mechanism operates at the chromatin surface, where inner nuclear membrane proteins such as LEM2 enhance BAF's DNA-binding affinity and increase the cross-link density of the resulting hydrogel network. These interactions form a pre-stressed surface hydrogel that can dynamically resist applied mechanical stress, thereby preserving chromatin integrity (Fig. 4e).

Together, this uncovers a novel design principle in which multivalent protein networks assemble on DNA polymers to buffer mechanical damage and enhance structural resilience – a strategy reminiscent of load-bearing tough hydrogels in material science[50,51]. Given the interconnected architecture of the inner nuclear membrane, this mechanism likely extends beyond BAF–LEM2 to include other LEM domain proteins[18], IDR-containing inner nuclear membrane proteins such as lamins or lamin B receptor[52–54], and even chromatin itself [9,46,55]. Lastly, the ability of DNA–protein co-condensation to generate biologically relevant forces suggests a broader dynamic role of condensates in shaping functional chromatin structures during processes such as transcription and replication [56–59].

Acknowledgments: We thank Jose Alberto Morin for the initial experiments on this system with the optical tweezer. We thank Tony Hyman, Anatol Fritsch and Juan Iglesias for help with phase separation saturation concentration determination, and Martin Beck and Reiya Taniguchi for sharing cryo electron tomography data. We thank the staff and students of the 2023 MBL Physiology course where important theory, initial experiments but no controls were performed, particularly A. Ortega Granillo, J. Brzostowski, N.King, and D. Fletcher. A.v.A., S.W.G. and F.J. acknowledge funding by the Max Planck Society. A.v.A. thank the European Research Council (Organelloids 101117619), German Research Foundation (SPP2191) for support. R.A. received support given by the Heineman Foundation through Minerva. F.J. acknowledges funding from the Volkswagen Foundation. We thank the following services and facilities at MPI-CBG Dresden for their support: Protein Expression Facility, Biophysics Core facility, Scientific Computing Facility, Genome Engineering Facility and the Light Microscopy Facility.

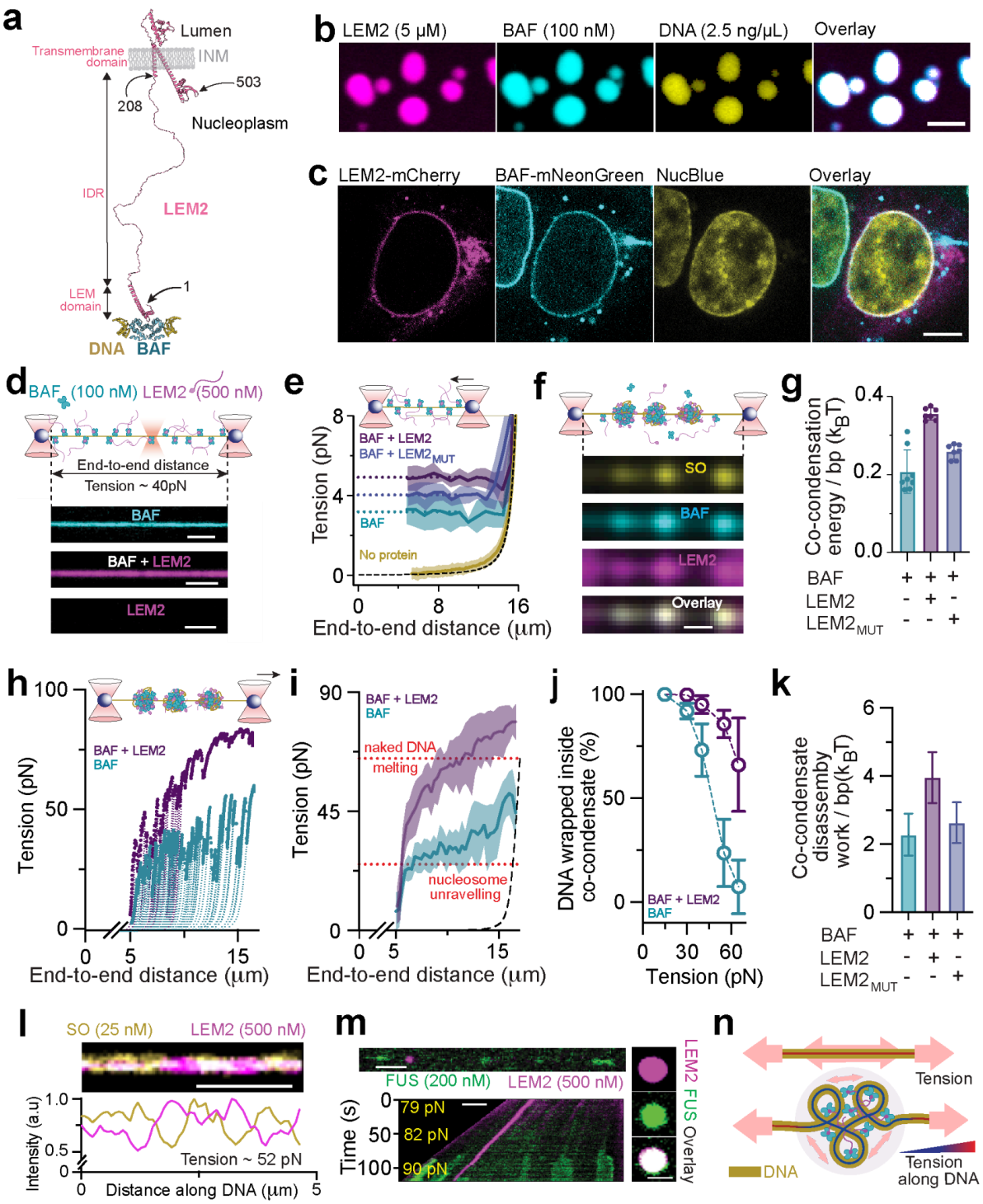

Fig. 1 : Co-condensation with BAF-LEM2 shields DNA beyond the melting transition.

a, DNA-BAF-LEM2 interfaces the chromatin surface with the INM. Numbers indicate amino acid positions.

b, Confocal imaging reveals bulk phase separation of reconstituted DNA-BAF-LEM2 (methods).

c, Confocal imaging of BAF, LEM2 and DNA in the nucleus shows enrichment at the nuclear envelope (methods).

d, Top, schematic of the optical tweezers assay where a single λ-DNA molecule is held between two optically trapped beads (large red cones with spheres) via biotin–streptavidin interactions at a tension of ~40 pN. Confocal imaging (small red cone) reveals BAF and LEM2 association to the stretched DNA. Bottom, confocal images of BAF (top), BAF and LEM2 (middle) and LEM2 (bottom) association to stretched λ-DNA.

e, Average tension vs. end-to-end distance graphs obtained with the optical tweezer by gradually reducing DNA end-to-end distance from 16.7 μm to 5 μm (top inset) reveals a constant tension plateau indicative of protein-DNA co-condensation of DNA with BAF (n = 8), with BAF+LEM2$_{MUT}$ (n = 7), and with BAF+LEM2 (n = 7; methods). Solid colored lines, average tension; colored shaded regions, mean ± standard deviation; dotted lines, extrapolations of tension to zero end-to-end distance; dashed black line, worm-like-chain (WLC) model of λ-DNA elasticity (methods).

f, Schematic representation (top) and representative example from **e** (bottom) of DNA-BAF-LEM2 co-condensates, DNA (yellow) is labelled with Sytox Orange (SO). Scale bar, 0.5 μm.

g, Co-condensation energy per DNA base pair (bp) obtained by integration of the tension vs. distance curves in **e**. Co-condensation energy is significantly higher for DNA-BAF-LEM2 than for DNA-BAF and DNA-BAF-LEM2$_{MUT}$.

h, Representative tension vs. end-to-end distance graphs (solid dots) obtained by gradually increasing DNA end-to-end distance from 5 μm to ~16.5 μm (top inset) reveals characteristic 'rip patterns', with each rip unraveling extended amounts of DNA, during DNA-BAF and DNA-BAF-LEM2 co-condensate tension-induced disassembly. Dotted lines, WLC fits (methods) reveal the contour length of DNA inside co-condensates (see **j**).

i, Corresponding average tension vs. end-to-end distance graphs for DNA-BAF (n = 10), and DNA-BAF-LEM2 (n = 10; methods) co-condensate tension-induced disassembly. Solid colored lines, average tension; colored shaded regions, mean ± standard deviation. DNA-BAF co-condensates disassemble at tensions slightly higher than those required to dissociate nucleosomes from DNA, while disassembling DNA-BAF+LEM2 co-condensates requires tensions above the critical melting tension of 65 pN. Dashed black line, WLC model of λ-DNA.

j, Fraction DNA remaining co-condensed during tension-induced disassembly as a

function of applied tension. Note that 66±22 % of DNA remains co-condensed with BAF+LEM2 at the critical melting tension of 65 pN.

k, Co-condensate per-base pair disassembly work obtained by integration of the tension vs. distance curves in **i** (BAF and BAF-LEM2) and Extended Data Fig. 3e,f (BAF-LEM2$_{MUT}$; n=5).

l, Top, confocal image of SO, bright in directions of high DNA tension and dim in regions of low DNA tension, at 52 pN DNA tension reveals that DNA tension is higher outside co-condensates than inside. Bottom, corresponding profiles of normalized intensities showing alternate low and high distributions.

m, Left, representative image (top) and kymograph (bottom) of DNA-BAF-LEM2 co-condensate disassembly under high tension reveals that the ssDNA binding protein FUS (green) exclusively associates with non-co-condensed regions, revealing that DNA inside co-condensates is protected from melting. Right, FUS partitions into LEM2 condensates in bulk, indicating that FUS is not excluded from DNA-BAF-LEM2 co-condensates.

n, Sketch of the IDR-dependent mechanism of co-condensate tension buffering. DNA tension (pink arrows) is reduced within co-condensate (bottom) as compared to without (top), since inside tension redistributes through IDR-IDR and other molecular interactions. Arrow thickness indicates relative tension strength, and direction shows the path of redistribution. Color bar represents tension magnitude along the DNA.

Scale bar, 5 μm in **b, c, m-**right and 2 μm in **d, l, m-**left**.**

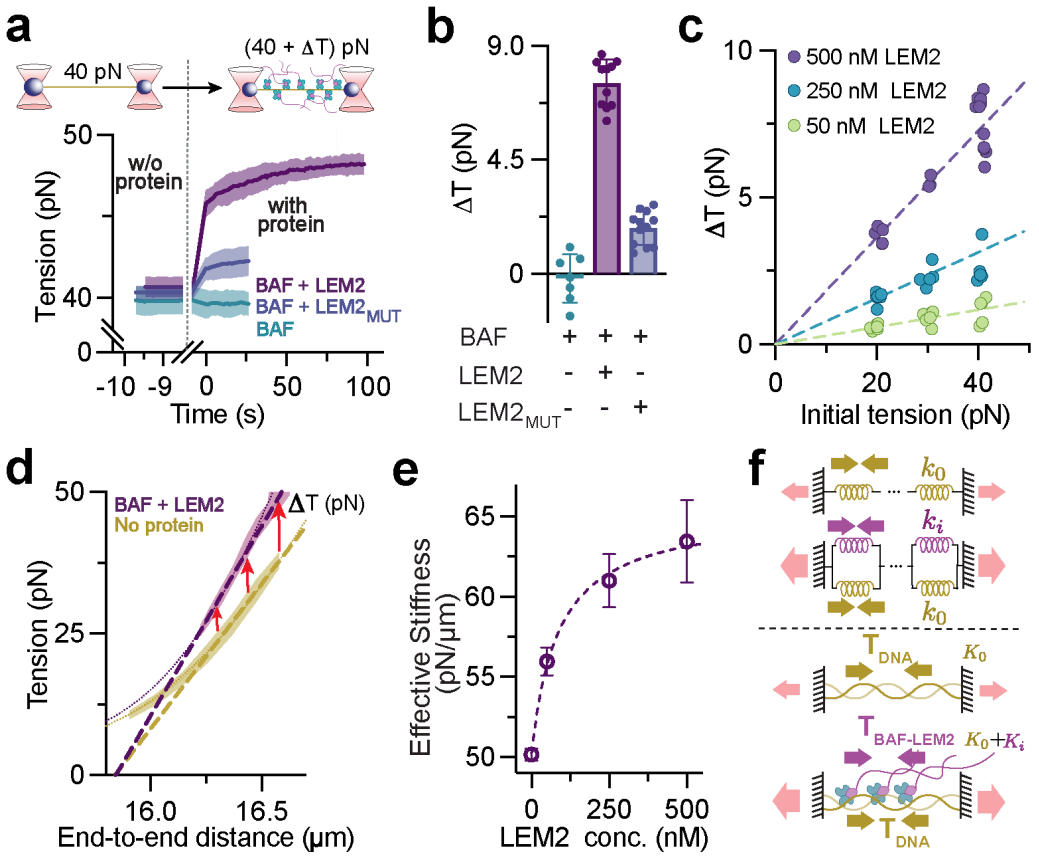

Fig. 2 : BAF-LEM2 assembly on DNA generates a reinforcing response.

a, Top, DNA stretched to an initial ~40 pN tension is subjected to a buffer exchange from protein-free (left) to protein-containing (right) at time t = 0s while trap positions are maintained. Bottom, tension increases with time post addition of 100nM BAF + 500nM LEM2 (BAF+LEM2) and 100nM BAF + 500nM $LEM2_{MUT}$ (BAF+$LEM2_{MUT}$) due to module assembly on DNA, but does not increase post addition of 100nM BAF alone. Solid colored lines, mean tension; colored shaded regions, mean ± standard deviation (BAF: n=7, BAF-LEM2: n=11, BAF-$LEM2_{MUT}$: n=12).

b, Corresponding average tension increases ΔT.

c, ΔT as a function of initial DNA tension and LEM2 concentration (100nM BAF, n=20 for 500nM LEM2, n=17 for 250nM LEM2, : n=19 for 50nM LEM2). Dashed lines, linear fit to the data within 95% confidence interval.

d, Direct experimental characterization of BAF-LEM2 module compliance in the enthalpic regime of DNA stretching via average tension vs. DNA end-to-end distance graphs in absence (yellow shaded region, mean ± standard deviation, n=11) and in presence (magenta shaded region, mean ± standard deviation, n=11) of 100nM BAF and 500nM LEM2. Dotted lines, WLC model of λ-DNA. Linear fits (dashed lines) in the enthalpic regime (methods) reveal a stiffness but not a rest-length change between

the two conditions (see main text). Red arrows illustrate tension increase ΔT when keeping DNA end-to-end distance fixed.

e, Effective stiffness as a function of LEM2 concentration (100nM BAF) measured via constant tension experiments (Extended Data Fig. 4c, methods). Error bars, mean ± standard deviation; dashed line, fit to the stiffening reinforcement model.

f, Sketch of the IDR-dependent mechanism of assembly-induced stiffening reinforcement. Top, DNA, represented as a series of springs (stiffness k_o), is held in place at fixed end-to-end distance. BAF-LEM2 module assembly results in the addition of springs in parallel (stiffness k_i). Saturated BAF-LEM2 binding increases the effective stiffness of the system from K_0 (DNA alone) to $K_0 + K_i$. Bottom, Saturated BAF-LEM2 binding and compliant element assembly generates tension $T_{BAF\text{-}LEM2}$ (magenta arrows) in addition to DNA tension T_{DNA} (yellow arrows), increasing the total tension experienced by the system (pink arrows).

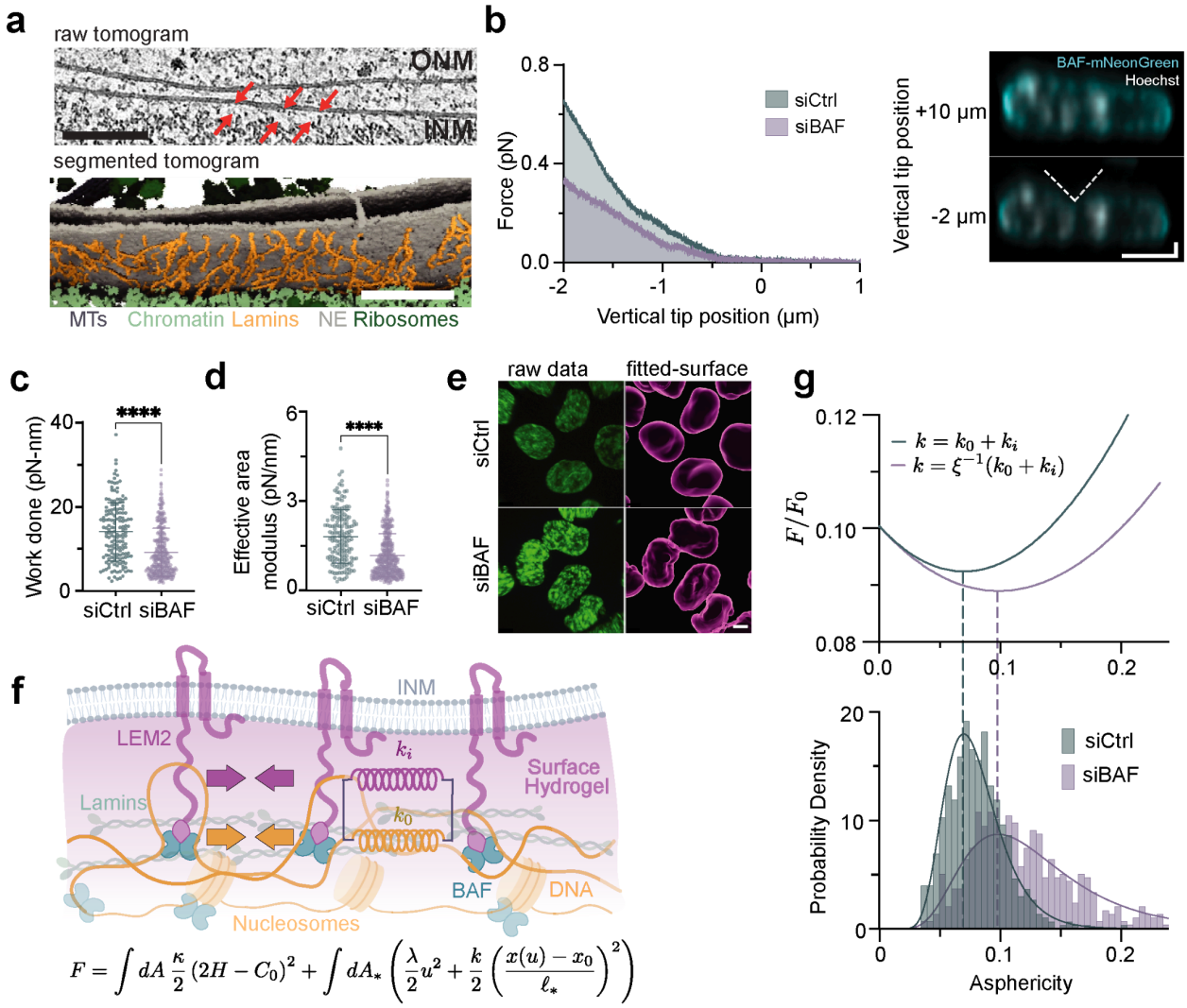

Fig. 3: A nuclear surface hydrogel.

a, Cryo-electron tomography of the nuclear envelope from [43], here reprocessed and reanalyzed. Top, representative slices from reconstructed tomogram revealing an amorphous layer beneath the INM approximately 14 nm thick (region between two red arrows). Bottom, 3D segmentation highlighting the lamin network, chromatin, nuclear envelope, microtubules (MTs), and ribosomes. Chromatin was cropped from the top to reveal the lamin network. Scale bar, 200 nm.

b, Left, representative AFM force-indentation curves of nuclei of latrunculin A-treated HCT-116 cells, for siCtrl and siBAF cells. The cantilever makes contact with the nucleus at a vertical tip position of 0 μm, and we measure the mechanical work (shaded areas under the curves) required to indent the nucleus by 2 μm. Indentation in absence of BAF requires less work than in presence. Right, representative live-cell images of an HCT-116 BAF-mNeonGreen cell not indented (Vertical tip position +10 μm) and

indented (Vertical tip position -2 μm). Segmentation of the nuclear surface reveals the nuclear surface area increase, which together with the mechanical work (**c**) allows for determination of the effective area modulus shown in (**d**) (methods). Dashed white line, illustration of pyramidal cantilever tip. Scale bar, 5 μm (horizontal and vertical).

c, Mechanical work for a 2 μm indentation of the nucleus of siCtrl and siBAF cells (methods), from three biological replicates (siCtrl: n = 159, siBAF: n = 319).

d, Effective area modulus of nuclei of control and siBAF cells (Extended Data Fig. 8b; siCtrl: n = 159, siBAF: n = 319, methods).

e, Left, Confocal image stacks of chromatin (NucBlue) of siCtrl (Top) and siBAF (Bottom) cells. Right, 3D segmentations of the nuclear surfaces for determining nuclear volume, shape, and surface area.

f, Top, Schematic of the REMM surface hydrogel (purple shade) formed below the INM (gray), comprising LEM2 (magenta), BAF (cyan), lamin filaments (green), DNA (yellow) and nucleosomes, with reinforcing properties as described (elastic properties indicated by coloured springs, tension indicated by colored arrows). Bottom, surface hydrogel free energy (*F*) is given by the sum of two integrals. The first integral, taken over the total area (A), includes the bending energy term with bending modulus κ and average and spontaneous curvatures H and C_0. The second integral, over the strain-free area (A_*), combines a bare area elastic energy term representing lamins with bare elastic area modulus λ and surface strain u, and a DNA-BAF-LEM module term with stiffness k, stretch relative to rest length $x(u) - x_0$ with $x(u) = x_*\sqrt{1+u}$ and $x_* = x(0)$, and surface density of DNA-BAF-LEM module binding sites in the strain-free state $1/l_*^2$. (SI).

g, Top, Plots of the normalized free energy (F/F_0) of the REMM model (**f,** see methods) as a function of nuclear asphericity reveal that the minimum for the siBAF condition with $k = \xi^{-1}(k_0 + k_i)$ with measured stiffness ratio ξ (see SI) is placed at a larger asphericity than for the siCtrl condition with $k = k_0 + k_i$. Bottom, histograms of nuclear asphericity measured as in (**e**) for siCtrl and siBAF cells (n = 603 and n = 591, respectively, pooled across three biological replicates). Colored lines, log-normal fit. With REMM model parameters $\lambda = 0.07$ pN/nm, $A_* = 1.8\,A_V$, $\kappa = 0$, rest length mismatch $x_0/x_* = 0.74$ and energy scale $F_0 = \lambda A_*$. The histograms peak at the values that minimize the corresponding REMM surface hydrogel free energy *F* (dashed lines).

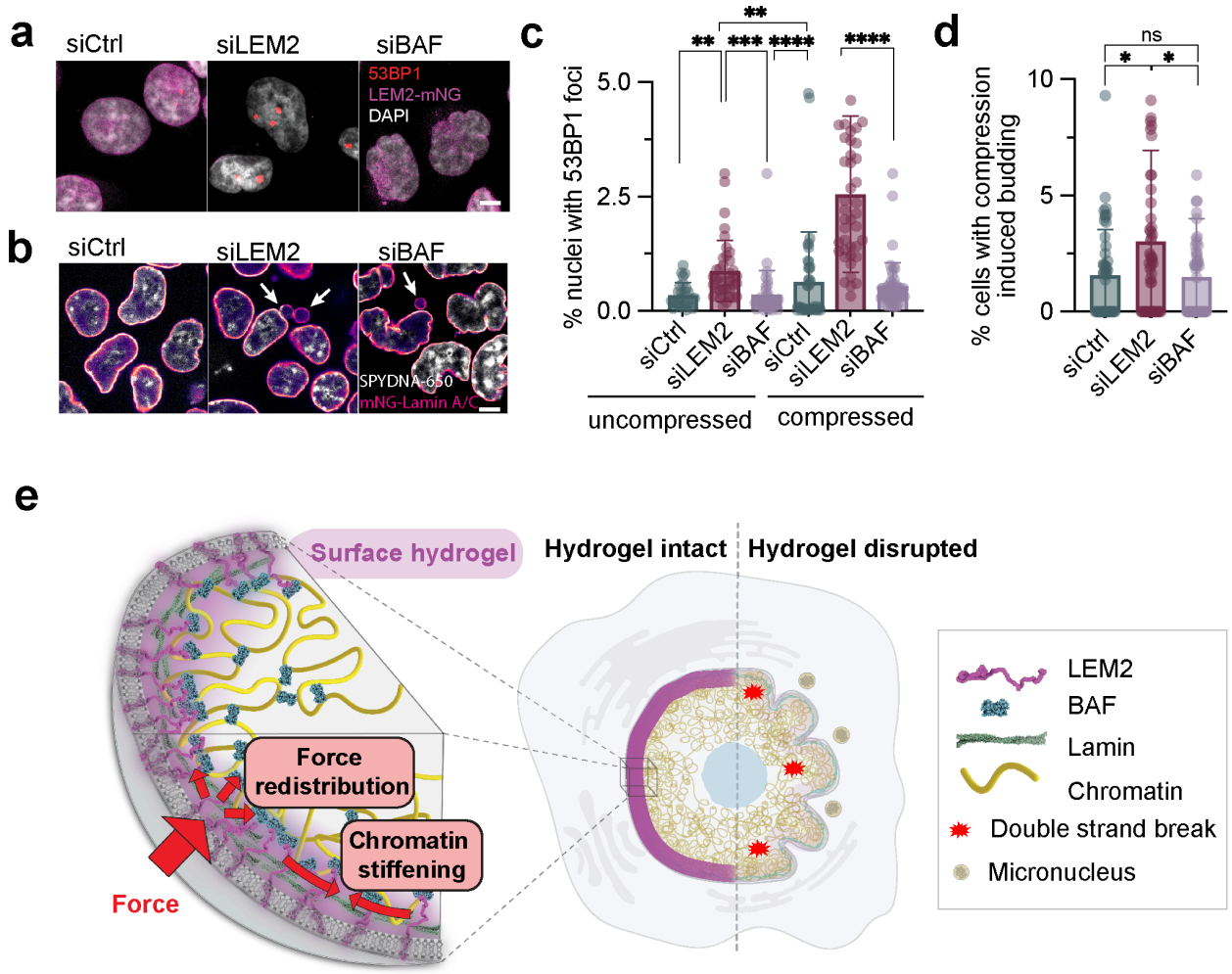

Fig. 4. Cellular functions of the BAF-LEM2 module.

a, Representative confocal images showing DNA damage loci visualized by immunofluorescence of 53BP1 in interphase HCT116 LEM2-mNeonGreen cells following siRNA treatments as indicated and compression to 6 µm. The compression induced mechanical strain results in DNA damage foci in siLEM2 cells.

b, Representative confocal images of live HCT116 LaminA/C-mNeonGreen cells with micronuclei (white arrows) following siRNA treatments and compression to 6 µm. The compression induced mechanical strain results in micronucleation in siLEM2 cells.

c, Percentage of nuclei that form 53BP1 DNA damage foci following siRNA treatments as indicated and remain uncompressed or are compressed to 6 µm (see **a**; three biological replicates, uncompressed: n = 26, 38, 34; compressed: n = 39, 41, 52 fields of view for siCtrl, siLEM2 and siBAF respectively). DNA damage increases ~2.2 fold in siLEM2 cells with compression compared to without compression. Non-significant comparisons are not shown.

d, Percentage of cells that form micronuclei following siRNA treatments as indicated and compression to 6 μm (see **b**, three biological replicates, siCtrl: n = 48; siLEM2: n = 54; siBAF: n = 53).

e, The REMM surface hydrogel model and its effect on the nuclear periphery and nuclear homeostasis.

Bars and whiskers represent mean ± s.d respectively. Scale bar, 5 μm. Statistical test used is Kruskal-Wallis test with multiple comparisons using Dunn's method (**c,f**). One-way ANOVA with multiple comparisons. * $p < 0.05$, ** $p < 0.005$, *** $p < 0.001$, **** $p < 0.0001$, ns: non-significant.

INM Proteins	Copy number	Average spacing (nm)
BAF dimers*	3.64×10^5	37
LEM2	8.20×10^4	79
Other LEM proteins	2.14×10^6	15
Lamin A/C	3.60×10^5	38
Lamin B dimers	1.71×10^6	17

Table 1. Average spacing of INM proteins

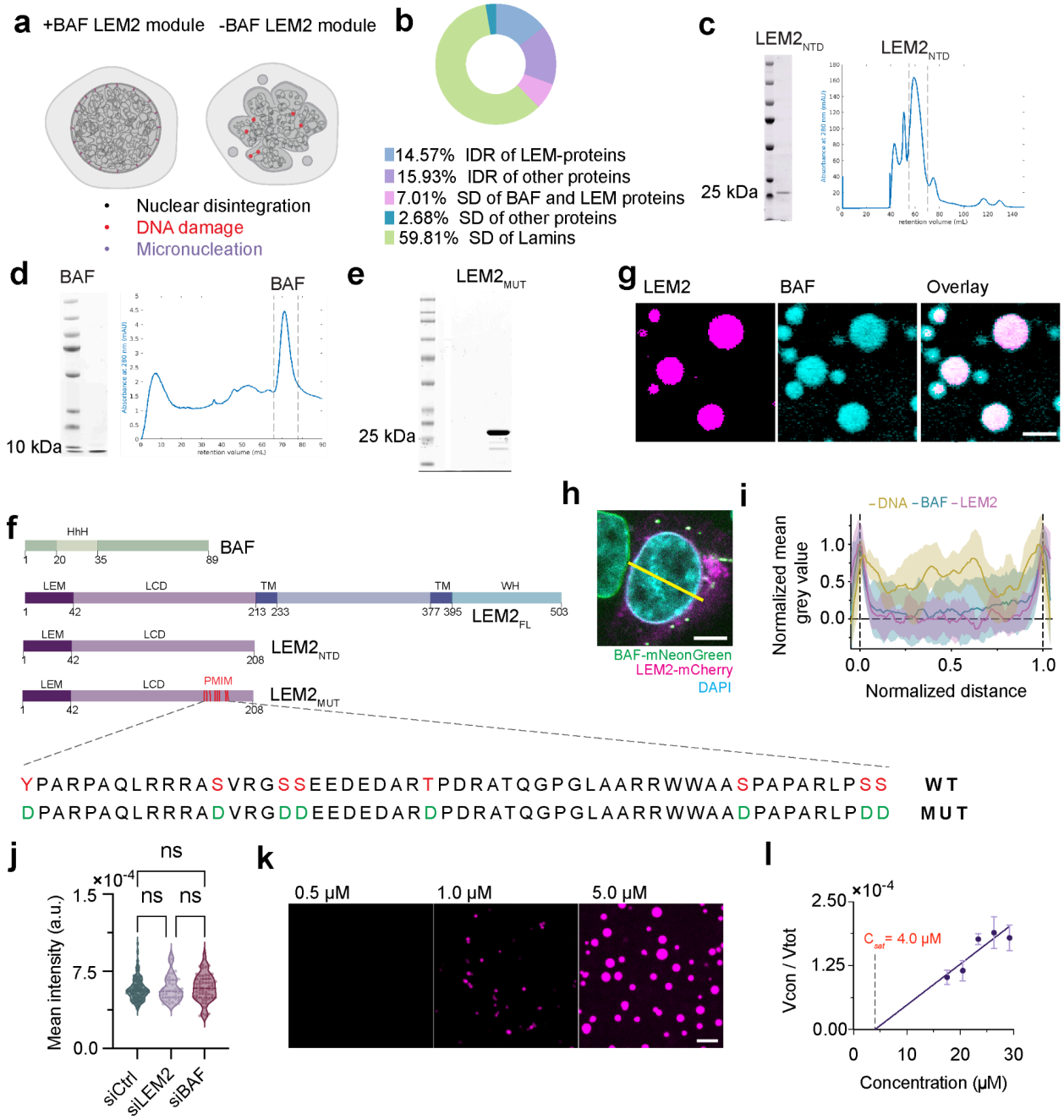

Extended Data Fig. 1 : A bottom-up reconstitution system for *in vitro* assembly of DNA-BAF-LEM2, with corresponding cellular visualization.

a, Schematic representation of nuclear disruption phenotypes when BAF-LEM2 is depleted. **b,** Composition of the nuclear lamina, highlighting structured domains (SD) and intrinsically disordered regions (IDR) of its constituent proteins. SDS PAGE (left) and SEC Elution profile (right) of purified recombinant **c,** LEM2 **d,** BAF. **e,** SDS PAGE of

purified recombinant $LEM2_{MUT}$. **f.** Domain chart showing protein domains of various recombinant constructs. Labels indicate domain names, and numbers represent amino acid positions. The red vertical lines indicate phosphomimetic mutations (PMIM; S,Y,T → D) introduced in LEM2 to abolish multivalent interactions. Full length LEM2 ($LEM2_{FL}$) is shown as reference. **g,** Bulk co-condensation assay of LEM2 and BAF showing enrichment of BAF in LEM2 condensates. **h,** Normalized averaged line intensity profiles of BAF, LEM2 and DNA across nuclei (left, red line) for different cells plotted as mean ± sd (right). **j,** Quantification of mean pixel intensity of DNA in the nuclear rim across knockdowns (N= 368, 220, 196 for siCtrl, siLME2 and siBAF respectively) indicating that the enrichment of DNA does not change with depletion of BAF or LEM2. Vertical lines in the violins show median and the interquartile ranges. **k,** Confocal images showing bulk phase separation upon concentration titration of LEM2. **l,** Assay of condensate volume fraction to determine C_{sat} for LEM2 (n=33,34,47,43,32 for input protein concentrations 17.58μM, 20.51μM, 23.44μM, 26.37μM, 29.29μM respectively, methods). Bars and whiskers represent mean ± s.d respectively. Scale bar, 5 μm. Statistical test used is Kruskal-Wallis test with multiple comparisons using Dunn's method. * $p < 0.05$, ** $p < 0.005$, *** $p < 0.001$, **** $p < 0.0001$, ns: non-significant.

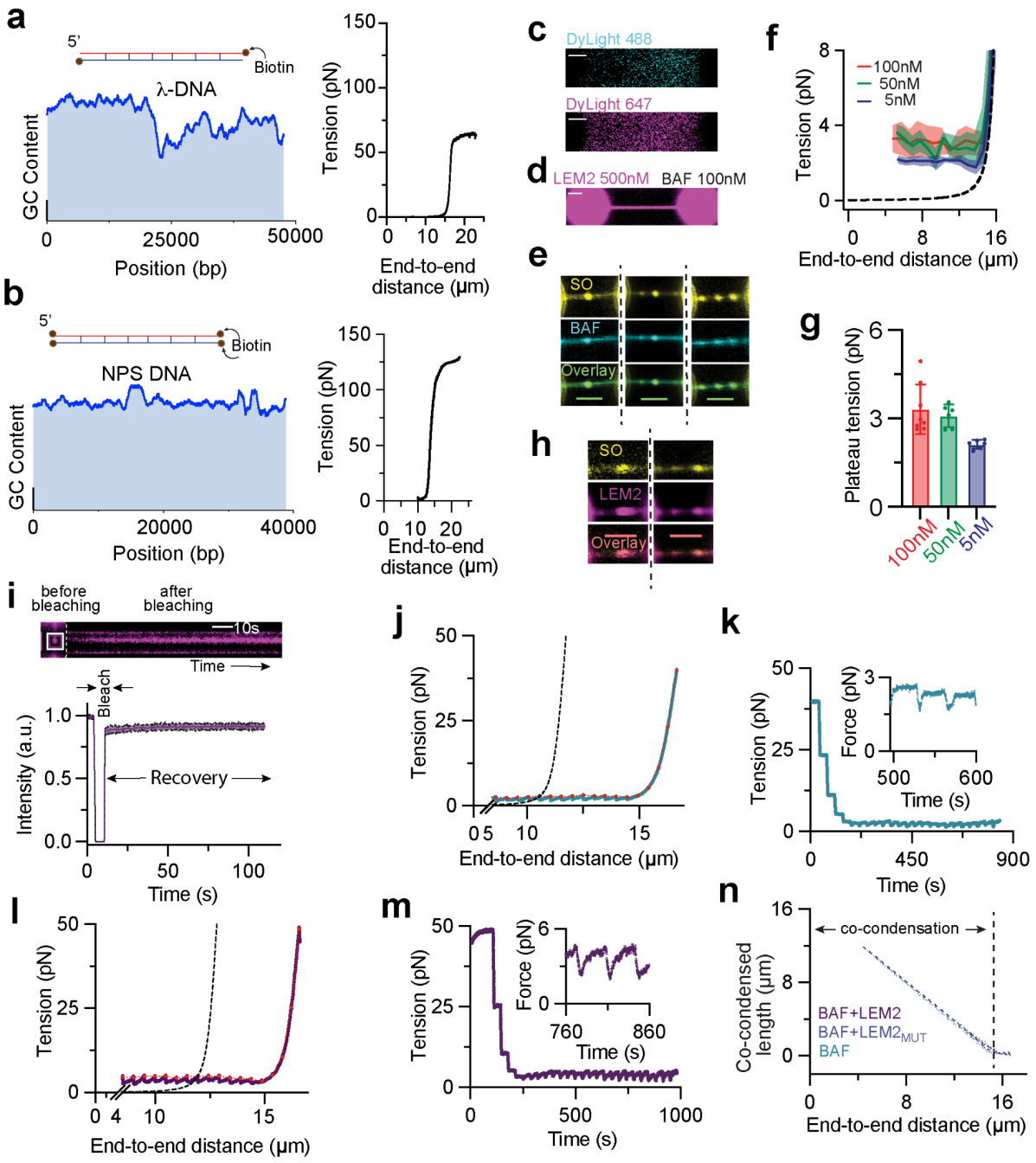

Extended Data Fig. 2 : Reconstitution of DNA-BAF-LEM2 co-condensate in optical tweezers.

a,b, Schematic diagrams and GC content profiles (Scale bar, 10%) of biotinylated (a) λ-DNA and (b) NPS DNA (left), with corresponding tension-extension curves (right). **c,** Confocal images of control experiment to test binding of the free chemical dye to DNA (tethered between beads), **d,** Confocal image of binding of LEM2 (labeled)+BAF to NPS

DNA. **e,** One or more co-condensates of DNA and BAF in optical tweezer with 100nM BAF (fluorescently labelled). **f,** Average tension-distance profiles of DNA with different concentration of BAF while the end-to-end distance is decreased suggesting that BAF binding to DNA saturates around 100 nM. Black dashed line indicates the eWLC fit. Data is plotted as mean±sd (n=8 for 100nM, n=6 for 50nM, n=6 for 5nM). **g,** The corresponding quantification of plateau tension at 5 μm end-to-end distance from tension-distance profiles in f. **h**, Confocal images showing one or more co-condensates of DNA-BAF-LEM2 in optical tweezer, with 100nM BAF (unlabelled) and 500nM of LEM2 (fluorescently labelled). **i,** FRAP of BAF-LEM2 co-condensate in optical tweezer. Top, pre-bleach confocal slice and post-bleach kymograph of FRAP time course for DNA-BAF-LEM2 co-condensate (inside white ROI). Bottom, average recovery profile of normalized fluorescence intensity (n=7). **j,l,** Tension-distance profiles of DNA while the end-to-end distance is decreased in case of **(j)** BAF and **(l)** BAF-LEM2. Red lines indicate the steady-state values of force for each end-to-end distance. Black dashed lines represent eWLC fit to calculate the amount of co-condensed DNA (methods). **k,m,** Tension-time profiles of DNA while the end-to-end distance is decreased in case of **(k)** BAF and **(m)** BAF-LEM2. Inset shows the equilibration of force with time (methods). **n,** Quantification of total co-condensed DNA length as a function of end-to-end distances for BAF, BAF-LEM2 and BAF-LEM2$_{MUT}$ (BAF : n=8; BAF-LEM2: n = 7; BAF-LEM2$_{MUT}$: n = 7).

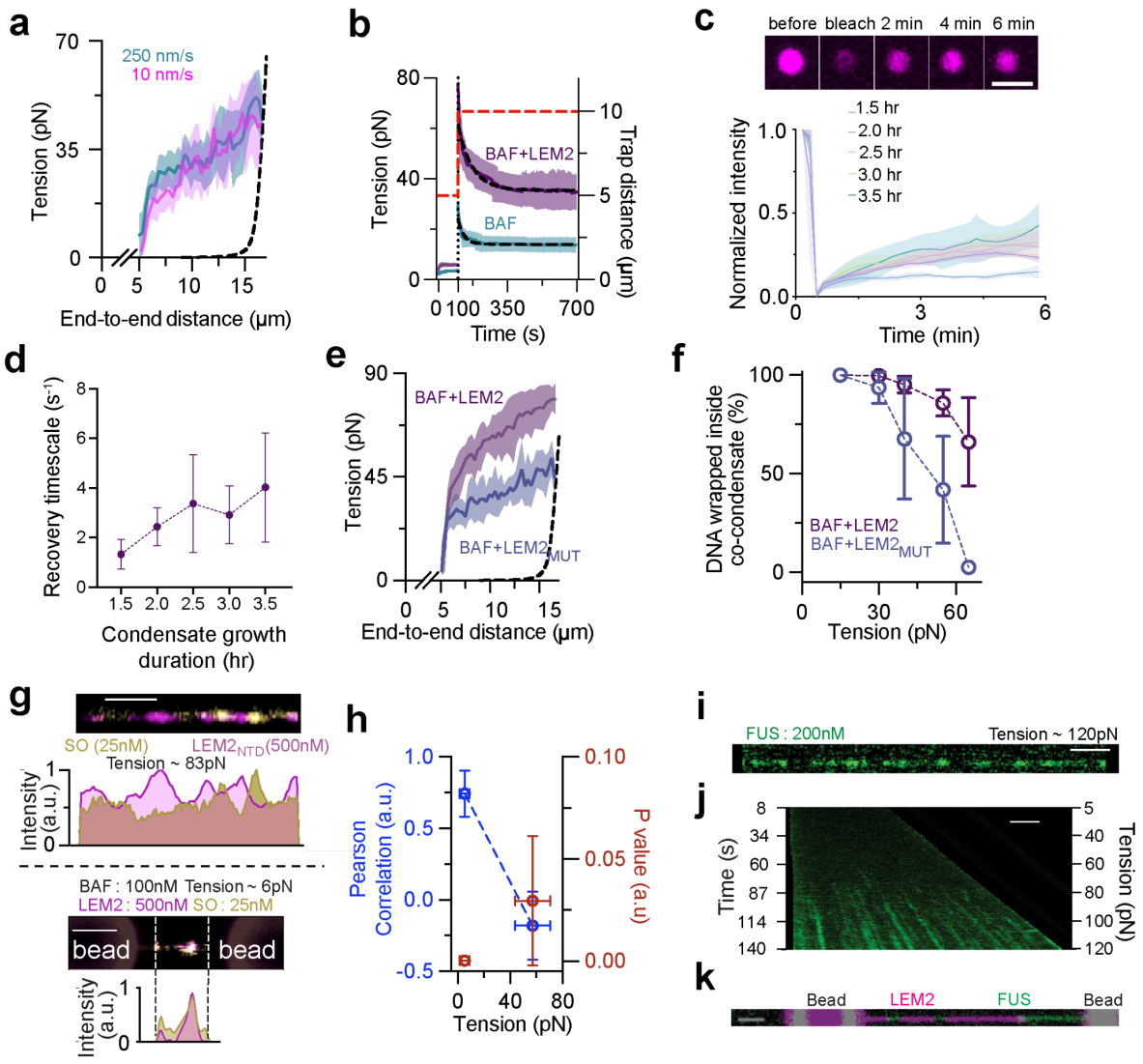

Extended Data Fig. 3 : DNA is protected inside DNA-BAF-LEM2 co-condensate.

a, The tension-distance profiles when the BAF co-condensates are disassembled as the end-to-end distance is increased at different speeds. **b,** Temporal tension relaxation profile following an instantaneous increase in trap-to-trap distance from 5 μm to 10 μm (BAF-LEM2:n=11, BAF:n=9, methods). **c,** FRAP of BAF-LEM2 co-condensate in bulk. Top: Confocal images showing fluorescence recovery after photobleaching (FRAP) of BAF-LEM2 condensates at indicated time points. Bottom, average normalized fluorescence recovery curves at different time points post-condensate formation (1.5 to 3.5 hours). Quantification shows mean ± s.d. of n = 5 replicates except for 2.0 hr, where

n = 4. **d,** The timescales of recovery of fluorescence intensity calculated from a simple exponential fit (methods) **e,** Average tension-distance profiles during co-condensate disassembly across multiple experiments for BAF-LEM2$_{MUT}$ (n = 5; BAF+LEM2 is replotted for reference). The dashed black line represents the eWLC fit for naked λ-phage DNA. **f,** Quantification of DNA wrapped inside the co-condensates as a function of applied tension (BAF+LEM2 is replotted for reference). **g,** Top, confocal image showing the binding pattern of SO on DNA in the presence of BAF-LEM2 co-condensates at high tension, with normalized intensity profiles of SO (yellow) and LEM2 (magenta) along the DNA (see methods). Bottom, co-localization of LEM2 and SO signal and corresponding normalised intensity profiles at low tension. Scale bar, 2 μm. **h,** Quantification of the Pearson correlation coefficient of LEM2 and SO signals at low tension (n=6) and high tension (n=8). **i,** Confocal slice showing the binding of FUS-GFP to ssDNA. **j,** Kymograph showing FUS-GFP signal emergence coinciding with melted ssDNA formation during DNA extension. **k,** Overlay of LEM2 (stains dsDNA) and FUS (stains ssDNA) signals on overstretched λ-DNA.

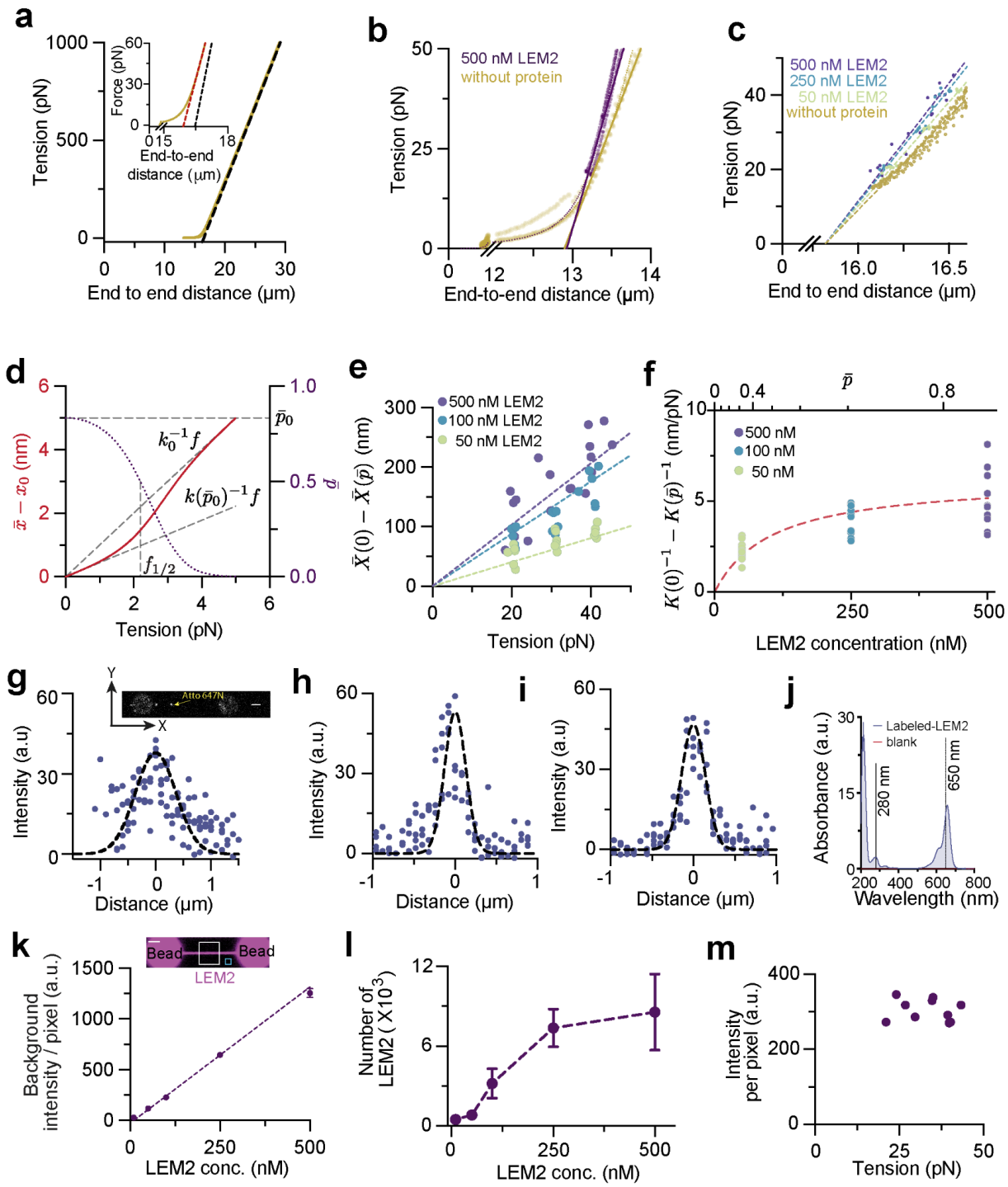

Extended Data Fig. 4 : DNA stiffness is modulated by the BAF-LEM2 module.

a, Asymptote (black dashed line) to the eWLC model (yellow line, for λ-DNA), indicating that the rest length is shorter than the contour length for linear fits (red dashed line,

inset) in the 20-40 pN range. **b,** Tension-distance profiles of NPS-DNA with (magenta) and without (yellow) BAF(100nM)-LEM2(500nM) while the end-to-end distance is increased. Dotted lines indicate the eWLC fits, whereas the dashed lines are linear fit to the respective data (methods) within 95% CI. (naked DNA:n=3, BAF-LEM2:n=3). **c,** Steady state end-to-end distance vs. tension for λ-DNA under a constant-tension protocol, across different LEM2 concentrations (with 100 nM BAF). Linear fits (dashed lines) show progressively higher stiffness with increasing LEM2 concentration (500 nM: n=18; 250 nM: n=18; 50 nM: n=17). **d.** Ensemble average stretch $\bar{x} - x_0$ per binding site (solid line) and average occupation fraction $\bar{p}$ (dotted line) as a function of applied tension on DNA (parameters used : k_0 = 1 pN/nm; k_i = 2 pN/nm; $c_0\exp(\beta\varepsilon)$ = 100 μM, c = 500μM, SI). Two regimes (at low and high tension) are shown by grey dashed lines with the corresponding stiffnesses k_0 and $k(\bar{p}_0)$ indicated. The half-saturation tension $f_{1/2} = \sqrt{2(\mu - \epsilon)k_0(1 + k_0/k_i)}$ is indicated as a vertical grey dashed line). **e**, Shortening of the end-to-end distance $\bar{X}(0) - \bar{X}(\bar{p})$ under constant-tension condition (from **c**) plotted against applied tension for varying LEM2 concentrations (with 100nM BAF). Dashed lines represent a global fit to the statistical mechanics model (SI). **f,** Change in DNA compliance $K(0)^{-1} - K(\bar{p})^{-1}$(from panel **e**) shown as a function of LEM2 concentration (with 100nM BAF). The red dashed line represents a global fit to the statistical mechanics model (SI). The top axis shows the corresponding occupation fraction. **g,** Quantification of the microscope's point spread function (PSF) from the intensity distributions of a single fluorophore. Individual points represent the maximum of pixel values along the x-y plane for each z-slice (methods). The solid line denotes the Gaussian fit. Inset, representative confocal image showing single Atto-647N dyes conjugated to λ-DNA. **(h-i)** Corresponding intensity distributions along (**h**) x and (**i**) y in the focal plane, used to determine the PSF in the x and y directions (n=5). **j,** The UV-Vis spectrum of labeled LEM2-DyLight 650 used to calculate the labeling efficiency (methods). **k,** Calibration of the mean background intensity as a function of input LEM2 concentration. Inset, representative confocal image showing LEM2 (tagged with DyLight-650) bound to DNA in optical tweezers. Cyan and white box indicate the ROIs used for background and DNA bound protein intensity quantifications (methods). **l,** Average number of LEM2 bound in presence of 100 nM BAF as a function of LEM2

concentration (**k,l** LEM2:500 nM n=11; LEM2:250 nM n=10; LEM2:100 nM n=7; LEM2:50 nM n=9; LEM2:10 nM n=12). **m,** Average pixel intensity, as a measure of total number of LEM2 bound to DNA across different forces for 100 nM BAF and 500 nM LEM2 (n=10).

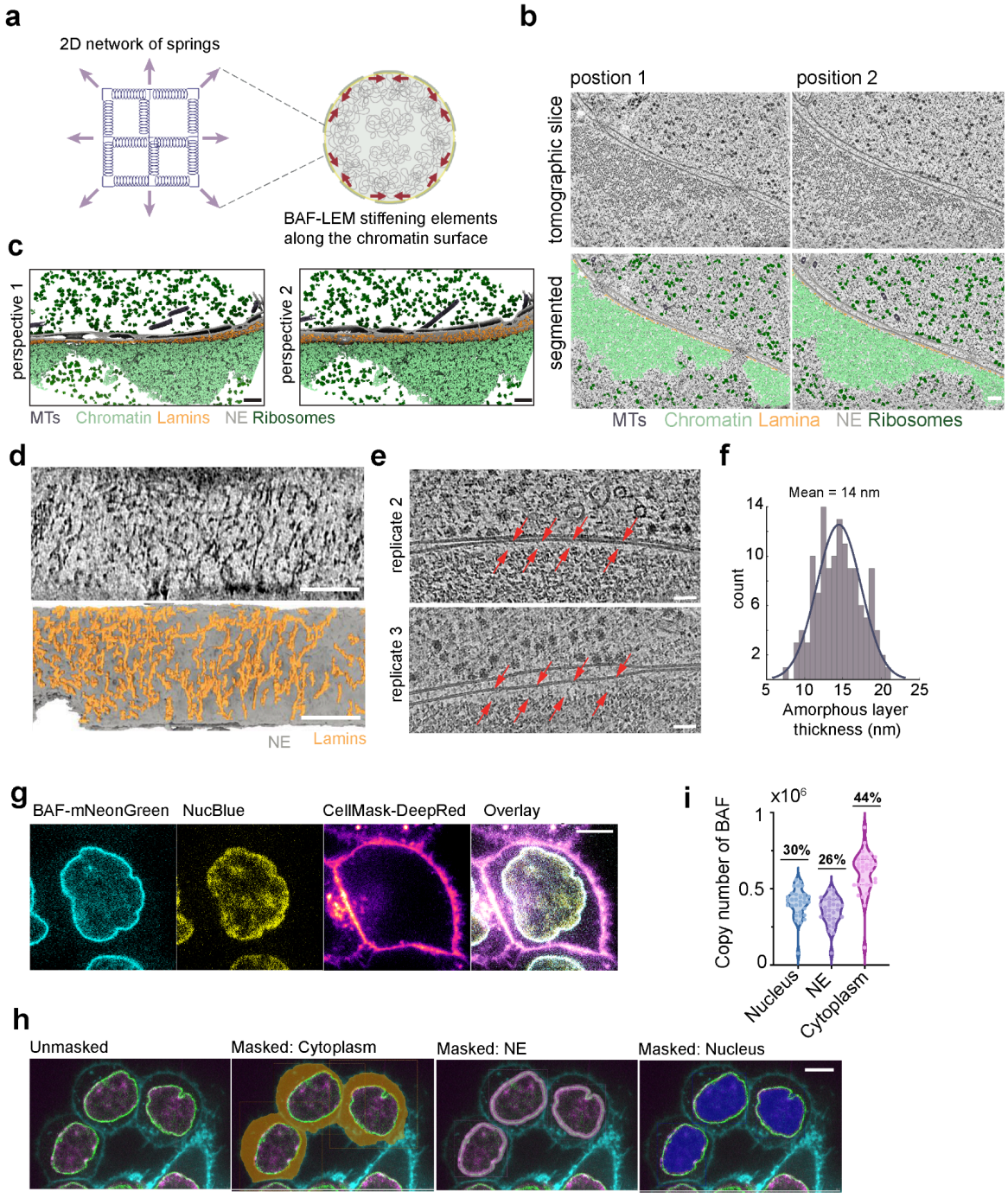

Extended Data Fig. 5 : Characterization of the nuclear lamina hydrogel and estimation of amounts of protein components.

a, Schematic showing the translation of individual springs to a 2D meshwork (left) representing the network of BAF-LEM2 around the chromatin surface (right). **b,**

Cryo-electron tomography of the nuclear envelope. Top**,** tomographic slices from different positions showing a continuous amorphous layer beneath the inner nuclear membrane. Bottom, the corresponding segmentations. **c,** 3D segmented models of the nuclear surface showing integration of lamin filaments into the hydrogel layer, flanked by INM and nucleosomes. Chromatin was cropped from the top to reveal the lamin network. Scale bar, 100 nm. **d,** Structural organization of lamin filaments inside INM. Top, cross-sectional view of the nuclear envelope showing lamin filaments embedded in the hydrogel layer. Bottom, segmentation of lamins. Scale bar, 100 nm. **e,** Zoomed-in view of tomographic slices from replicate tomograms showing the hydrogel layer (red arrows). Scale bar, 50 nm. **f,** Histogram showing the distribution of hydrogel thickness across tomograms, fitted with a normal distribution (mean thickness = 14 nm, n = 130). **g,** Confocal images showing the distribution of BAF in different cellular compartments, nucleus, nuclear envelope and the cytoplasm. Scale bar, 5 μm. **h,** Representative images showing the 3D segmentation of BAF pools in the cytoplasm, nuclear envelope and the nucleus. Scale bar, 5 μm. **i**, The average copy numbers of BAF in the three cellular pools of BAF: nucleus, NE and cytoplasm (n = 31 cells, methods).

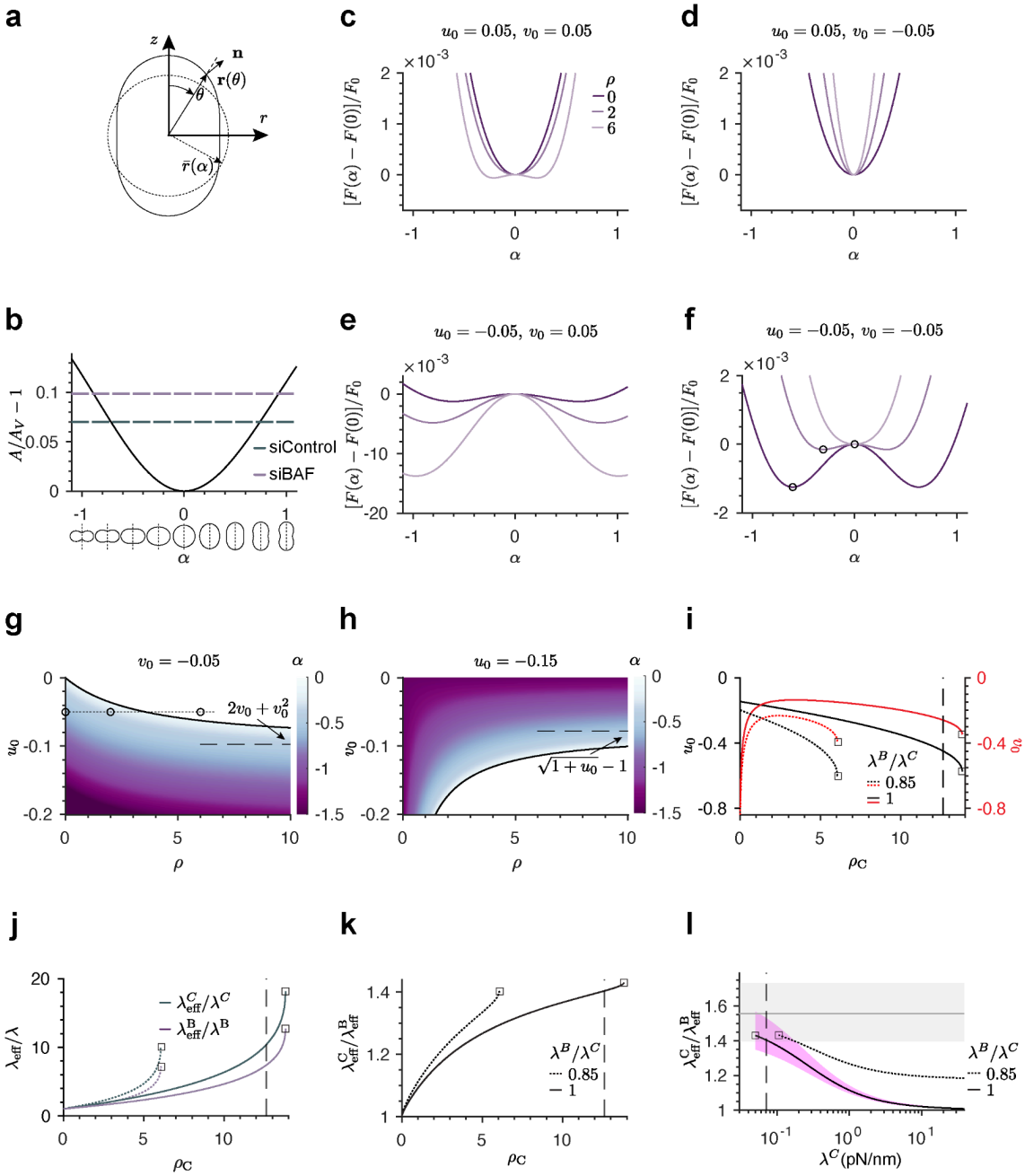

Extended Data Fig. 6 : Elastic surface hydrogel model.

a, Axisymmetric shape parametrization $r(\theta) = \bar{r}\,(1 + \alpha\, Y_{20})$ (black solid line), where θ is the axial angle relative to the z-axis, Y_{20} is the spherical harmonic with $l = 2$ and $m = 0$, α is the shape parameter, and the amplitude of $\bar{r}\,(\alpha)$ varies with α to ensure that the enclosed volume V is fixed for all shapes. Here, **n** denotes the unit normal vector to

the surface. Shape shown corresponds to $\alpha = 0.5$. **b,** Asphericity $(A/A_V - 1)$ shown as a function of α, where A is the surface area of the parametrized shape and $A_V = (6\sqrt{\pi}\,V)^{2/3}$ is the surface area of the sphere enclosing the same volume V. Shapes $r(\theta)$ shown for different values of α along the axis. Horizontal dashed lines indicate the asphericity values corresponding to the peaks of the distribution in Fig. 3g. **c–f,** Normalized free energy difference shown as a function of α for dimensionless BAF-LEM density ρ = 0, 2, 6 (dark to light color). The parameter values $u_0 = A_V/A_* - 1$ and the rest length mismatch v_0 are indicated, where A_* is the strain-free area. Circles in panel **f** indicate the energy minima corresponding to oblate shapes $(\rho = 0, 2)$ and to the sphere $(\rho = 6)$. Here, $F_0 = \lambda A_*$, where λ is the bare elastic area modulus. **g,h,** Phase diagrams in the u_0-ρ plane (left) and v_0-ρ (right) plane, where the color indicates the value of $\alpha < 0$, that minimises the free energy. The black critical line (SI, section II) marks the second-order transition between spheres and oblate shapes. Open circles connected by a dotted line correspond to the open circles in panel **f**. Horizontal dashed lines in **g,h** indicate the asymptotic limit of the critical line for large ρ. **i-k,** Parametric plots of parameters u_0 and v_0 (**i**), normalized effective stiffness λ_{eff}/λ (**j**), and ratio $\lambda_{eff}{}^C/\lambda_{eff}{}^B$ corresponding to the two experimental conditions siControl (C) and siBAF (B). Plots are shown as a function of $\rho_C = \rho$ with $\rho_B = (\lambda^C/\lambda^B)\,\xi^{-1}\rho$, $\xi = 1.41$ (95% CI 1.33–1.56), and λ^B/λ^C as indicated. For these values, minimum energy shapes have the asphericities indicated in panel **b. l,** Ratio of effective area moduli $\lambda_{eff}{}^C/\lambda_{eff}{}^B$ shown as a function of the bare area elastic modulus λ^C for two values of λ^B/λ^C, as indicated. The measured value (Fig. 3d) is shown as a grey line. Shaded bands mark the 95% CI. In **i-l,** vertical dashed lines mark the parameter choice used in Fig. 3**g**, open squares denote points where the solution ends.

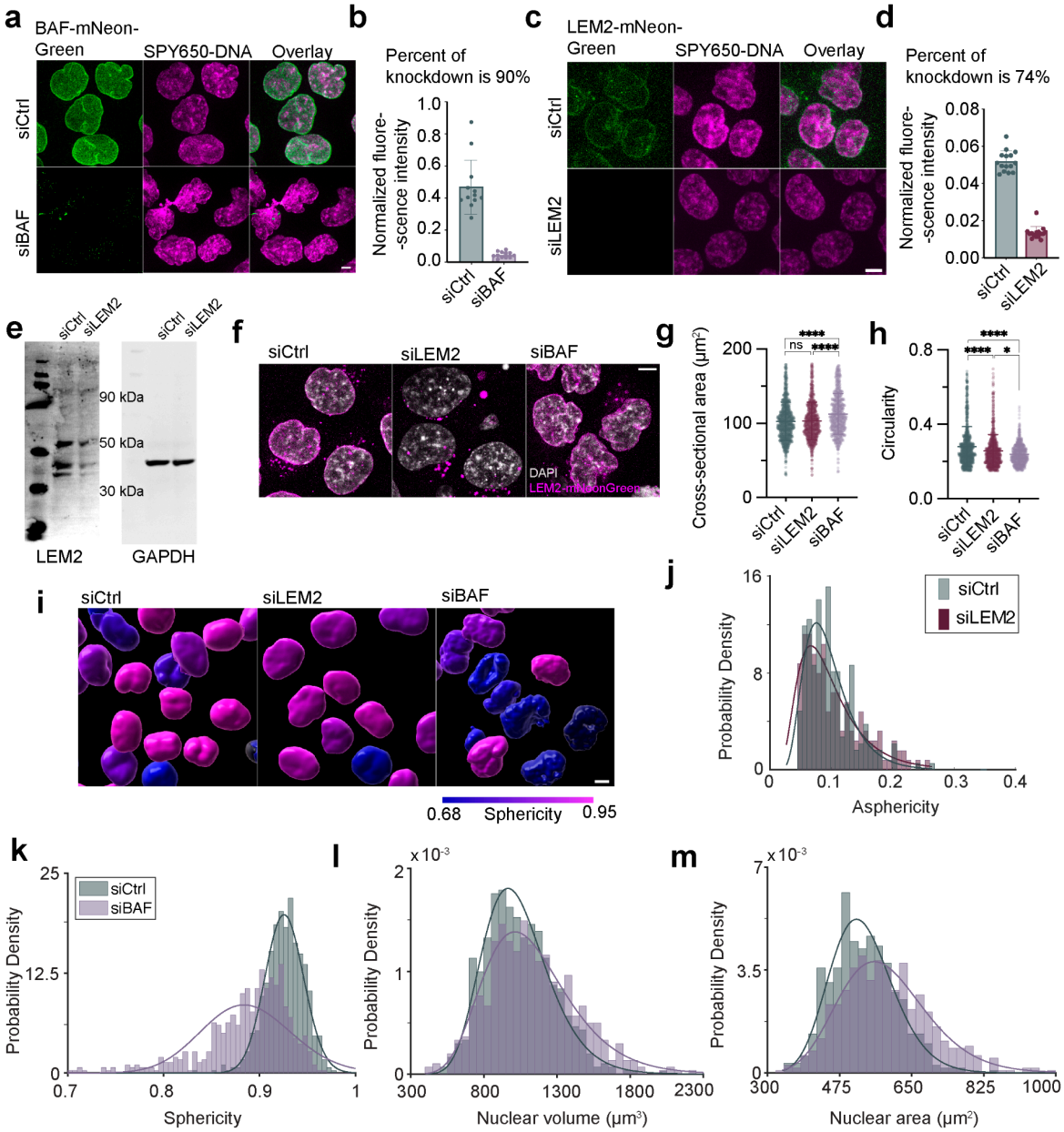

Extended Data Fig. 7 : Nuclear morphology breaks down upon BAF-LEM2 depletion.

a-d, Quantification of protein knockdowns. Confocal images showing loss of fluorescence upon (a) BAF knockdown, (c) LEM2 knockdown and (b,d) corresponding quantification of the extent of knockdown from fluorescence loss (siCtrl vs siBAF; n = 12 each, siCtrl vs siLEM2; n = 15 each, each point represents independent fields of view). **e,** Western blot showing depletion of LEM2 in HCT116-Lamin A/C mNeonGreen cells. GAPDH is a loading control. **f,** Maximum projection confocal images of nuclei across

knockdown showing morphology defects. **g-h,** Cross-sectional area (g) and circularity (h) of nuclei across knockdowns (siCtrl: n=973, siLEM2: n=790, siBAF: n= 720 cells, data pooled across three biological replicates). **i,** Representative image of 3D surfaces reconstructed on siCtrl and siBAF nuclei showing nuclear sphericity with a color gradient (colorbar labels indicate sphericity values). **j,** Histogram and corresponding lognormal fits of asphericity of siCtrl (0.0754±0.0050) and siLEM2 (0.0664±0.0066). siCtrl: n = 241, siLEM2: n = 163 cells. **k,** Histograms and corresponding lognormal fits of sphericity between siCtrl (0.9256±0.0020) and siBAF (0.8839±0.0042) **l,** Histograms and corresponding lognormal fits of nuclear volume between siCtrl (965±19 μm^3) and siBAF (1012±26 μm^3). **m,** Histograms and corresponding lognormal fits of the nuclear area between siCtrl (516±6 μm^2) and siBAF (556±9 μm^2). siCtrl: n = 603, siBAF: n = 591 cells, pooled across three biological replicates in **k,l,m.** Bars and whiskers / midline and whiskers in scatter plots represent mean±s.d. respectively. Scale bar, 5 μm. Statistical test used is Kruskal-Wallis test with multiple comparisons using Dunn's method. * $p < 0.05$, ** $p < 0.005$, *** $p < 0.001$, **** $p < 0.0001$, ns: non-significant.

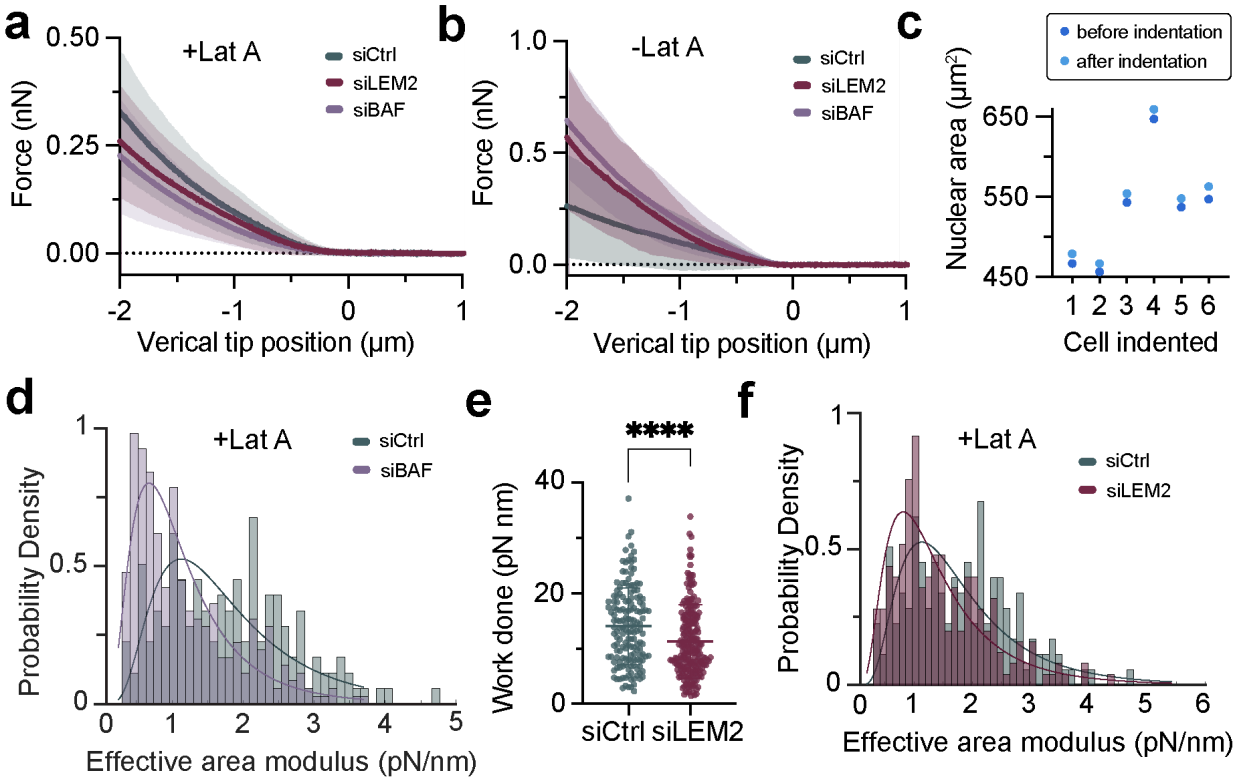

Extended Data Fig. 8 : Depletion of the BAF-LEM2 module lowers the effective area modulus of the nuclei.

a, Average force-indentation traces of nuclei across knockdowns in the presence of latrunculin A (siCtrl: n = 159, siLEM2: n = 225, siBAF: n = 319, data pooled across three biological replicates). **b,** Average force-indentation traces of nuclei across knockdowns in the absence of latrunculin A (siCtrl: n = 70, siLEM2: n = 57, siBAF: n = 170, data pooled across three biological replicates). Zero in the x-axis indicates the point at which the cantilever makes contact with the nucleus. **c,** The area change observed upon intending the nuclei with an AFM cantilever (until 2 µm) for 6 replicates. **d,** Histograms and corresponding lognormal fits of effective area modulus calculated from individual AFM curves in the presence of latrunculin A for siCtrl and siBAF (siCtrl: n = 159, siBAF: n = 319, data pooled across three biological replicates, methods). **e,** Work done calculated from individual AFM curves for siCtrl and siLEM2 (siCtrl: n = 159, siBAF: n = 225, data pooled across three biological replicates) **f,** Histograms and corresponding lognormal fits of effective area modulus calculated from individual AFM curves in the presence of latrunculin A for siCtrl and siLEM2 (siCtrl: n = 159, siBAF: n =

225, data pooled across three biological replicates). Bars and whiskers / midline and whiskers in scatter plots represent mean ± s.d respectively. Scale bar, 5 μm. Statistical test used is Kruskal-Wallis test with multiple comparisons using Dunn's method. * $p < 0.05$, ** $p < 0.005$, *** $p < 0.001$, **** $p < 0.0001$, ns: non-significant.

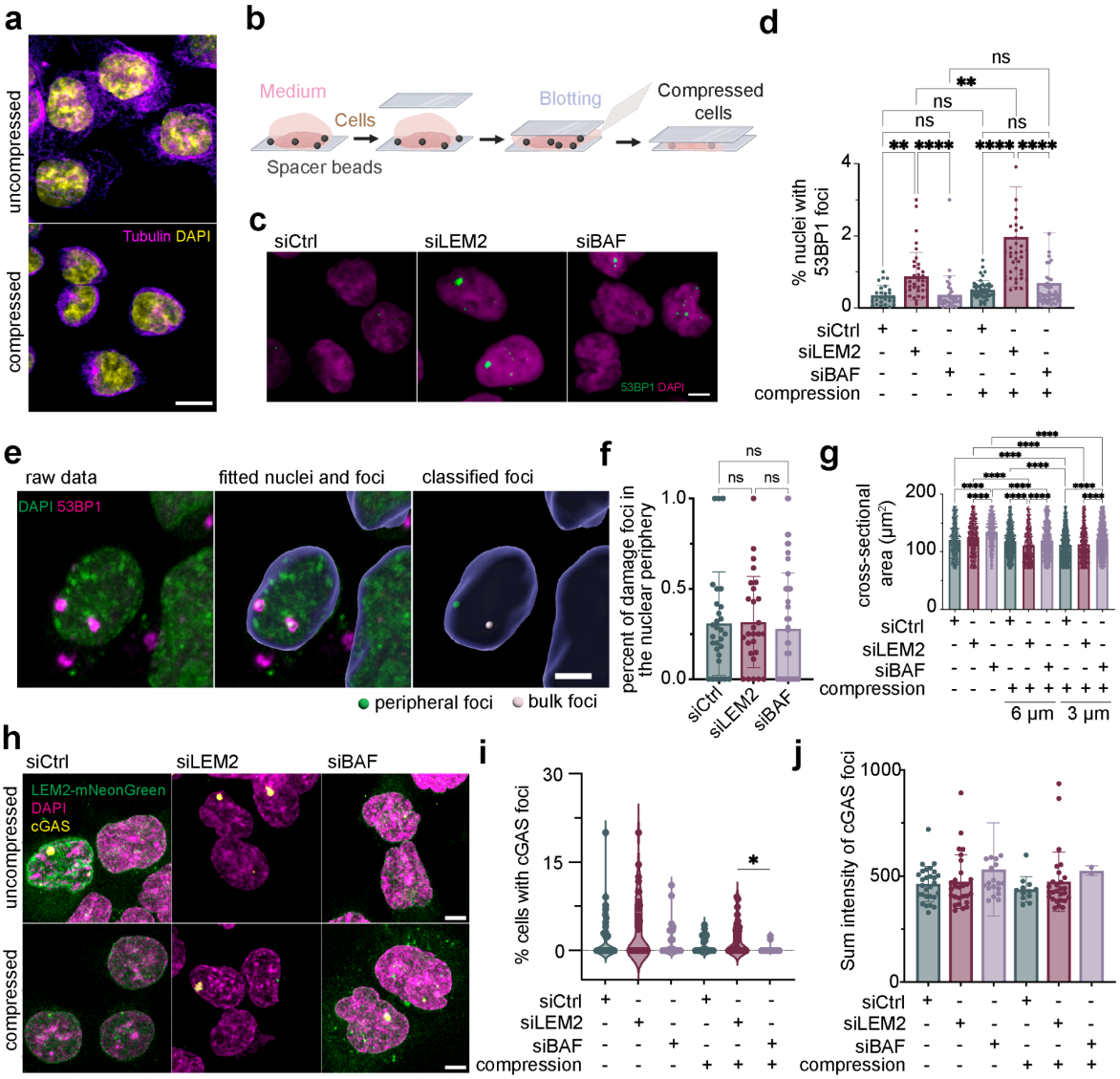

Extended Data Fig. 9 | Characterization of DNA damage and nuclear envelope rupture upon BAF-LEM2 depletion.

a, Maximum projection confocal images showing the loss of spindle architecture upon mechanical stress confirming compression of the nucleus. **b**, Schematic of the live cell compression protocol. **c,** Confocal images showing the accumulation of DNA damage foci upon compression of cells to a height of 3 µm. **d,** Quantification of percent of nuclei with DNA damage foci before and after compression from **c** (uncompressed: n=26, 38, 34 and compressed n=48, 42, 47 for siCtrl, siLEM2 and siBAF respectively. Data is pooled from 3 biological replicates.). **e,** Segmentation of DNA damage foci and

classification of foci to bulk or peripheral damage. **f,** Quantification of fraction of DNA damage occurs at the periphery of the nucleus compared to the total damage foci observed (siCtrl: n=29, siLEM2: n=27, siBAF: n=46, each point represents an independent field of view). **g,** Quantification of cross-sectional area of nuclei before and after compression across knockdowns from immunofluorescence (uncompressed: n=460, 572, 655; compressed until 6 μm: n= 1162, 504, 867; compressed until 3 μm: n=1599, 682, 1371 for siCtrl, siLEM2 and siBAF respectively). **h,** Maximum projection confocal images of nuclei with NER marked by cGAS foci, across knockdowns with and without compression. **i,** Quantification of percentage of cells with NER across conditions from **i** (uncompressed: n=36,35,39 and compressed: n=32,32,25 for siCtrl, siLEM2 and siBAF. Each point represents an independent field of view). **j,** Quantification of total intensity of cGAS foci in nuclei across conditions in **i**. All comparisons are non-significant. Bars and whiskers / midline and whiskers in scatter/violin plots represent mean ± s.d respectively. Scale bar, 5 μm. Statistical test used is Kruskal-Wallis test with multiple comparisons using Dunn's method. * $p < 0.05$, ** $p < 0.005$, *** $p < 0.001$, **** $p < 0.0001$, ns: non-significant. Non-significant comparisons are not shown in **g**,**i** and **j.**

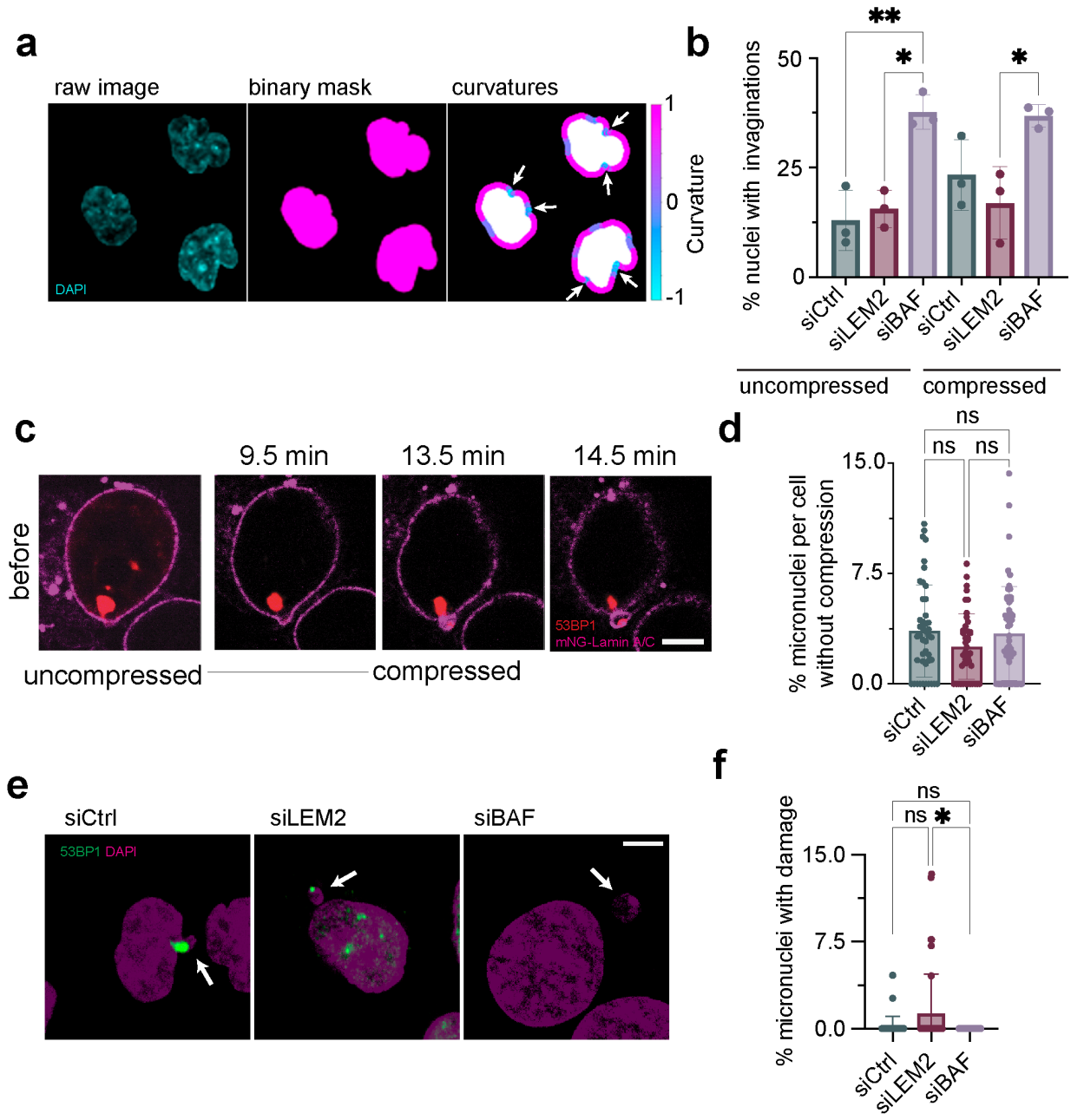

Extended Data Fig. 10 | Characterization of nuclear invaginations and micronucleation upon mechanical compression.

a, Representative confocal image of nuclei, corresponding binary mask and calculated contour curvatures used to quantify the invaginations into nucleus. White arrows indicate curvature patterns counted as invaginations (methods). **b**, Percentage of nuclei having invaginations of the nuclear envelope quantified across knockdowns across three biological replicates (uncompressed siCtrl: n=6,10,10; siLEM2: n=9,16,13; siBAF :

n =10,14,10, compressed siCtrl: n=17,11,10; siLEM2: n=19,11,11; siBAF: n=18,11,11). **c**, Confocal time course of DNA damage occurring live upon mechanical compression followed by the expulsion of a micronucleus. **d**, Quantification of percentage of cells with micronuclei before compression (siCtrl: n=44, siLEM2: n=44, siBAF: n=55, data pooled across three biological replicates with each point representing an independent field of view). **e**, Confocal images slices showing formation of micronuclei with DNA damage foci contained inside (arrows point to damage foci) after compression. **f**, Quantification of percentage of nuclei having a micronuclei containing DNA damage (siCtrl: n=37, siLEM2: n=41, siBAF: n=35, data pooled across three biological replicates with each point representing an independent field of view).Bars and whiskers represent mean ± s.d respectively. Scale bar, 5 μm. Statistical test used is Kruskal-Wallis test with multiple comparisons using Dunn's method. * $p < 0.05$, ** $p < 0.005$, *** $p < 0.001$, **** $p < 0.0001$, ns: non-significant. Non-significant comparisons are not shown in **b**.

Supplementary Information 1

Supplementary Table 1

Supplementary Information 2

Supplementary Movies

Table S1. Top, copy numbers and domain distributions of INM proteins. Bottom, categorized protein domain distributions in the INM.

Movie S1. Binding of BAF to DNA in optical tweezers. BAF, labeled with DyLight 488 NHS Ester (appearing cyan in the movie), binds to λ-phage DNA under ~40 pN of tension. The DNA was initially tethered between two beads in a buffer channel, then transferred to a protein channel containing 5% labeled BAF(100nM) in constant trap position mode. In the movie, the two beads appear as dark spots, while the stretched DNA is seen as a bright cyan horizontal line.

Movie S2. Binding of LEM2 to DNA in presence of BAF in optical tweezers. LEM2, labeled with DyLight 650 NHS Ester (appearing magenta in the movie), binds to λ-phage DNA under ~40 pN of tension in the presence of BAF (unlabelled). The DNA was initially tethered between two beads in a buffer channel, then transferred to a protein channel containing unlabeled BAF(100nM) and 1% labeled LEM2(500nM). In the movie, the two beads appear as bright blobs (due to unspecific binding of LEM2 to the bead surface), while the stretched DNA is seen as a bright magenta horizontal line.

Movie S3. LEM2 alone does not bind to DNA. LEM2, labeled with DyLight 650 NHS Ester (appearing magenta in the movie), does not bind to λ-phage DNA on its own. The DNA was initially tethered between two beads in a buffer channel, then transferred to a protein channel containing 1% DyLight-labeled LEM2 (500 nM). In the movie, only two bright fluorescent blobs are visible, corresponding to nonspecific LEM2 binding on the bead surfaces, with no signal along the DNA. To confirm the DNA tether, the left bead (held in a steerable optical trap) is brought close to the right bead and then retracted, allowing the DNA to relax and re-stretch, as shown by the tension-distance profile.

Movie S4. Formation of DNA-BAF co-condensates in optical tweezers. DNA initially held at 40 pN tension in a buffer-only channel was transferred to a channel containing BAF (100 nM, 5% fluorescently labeled, appearing cyan in the movie) and 25 nM Sytox Orange (appearing yellow in the movie). The steerable trap (left trap) was then moved to introduce slack into the DNA, resulting in the formation of DNA-BAF co-condensates. These appear as three bright puncta in the movie. The two beads appear as bright

yellowish-cyan blobs (due to unspecific binding of BAF/Sytox Orange to the bead surface).

Movie S5. Formation of DNA-BAF-LEM2 co-condensates in optical tweezers. DNA, initially held at 40 pN tension in a buffer-only channel was transferred to a channel containing BAF (100 nM, unlabeled), LEM2 (500 nM, 1% labeled, appearing magenta in the movie), and 25 nM Sytox Orange (appearing yellow in the movie). The steerable trap (left trap) was then moved to introduce slack into the DNA, resulting in the formation of DNA–BAF–LEM2 co-condensates, which appear as bright white puncta in the movie. The two trapped beads appear as bright blobs due to nonspecific binding of LEM2/BAF/Sytox Orange to the bead surfaces, predominantly from LEM2.

Movie S6. Melting of ds-DNA outside co-condensate. DNA with preformed DNA–BAF–LEM2 co-condensates was continuously stretched to disassemble the co-condensates in the presence of FUS (200 nM, GFP-tagged, appearing green in the movie). Magenta fluorescence corresponds to LEM2 (500 nM, 1% labeled), while BAF is unlabeled. The green FUS signal is observed only outside the magenta puncta representing the DNA–BAF–LEM2 co-condensates. The two large magenta blobs correspond to the trapped beads, due to nonspecific binding of LEM2 to the bead surfaces.

Materials & Methods

No statistical methods were used to predetermine sample size. The experiments were not randomized and, except where stated, investigators were not blinded to allocation during experiments and outcome assessment.

Section 1: Protein biochemistry and structure

A. Structure of LEM2 and NE protein distribution with AlphaFold

The LEM2 structure (Fig. 1a) was modeled using the published BAF-LEM assembly [47,60,61] and AlphaFold [62] predictions for remaining LEM2 domains (UniProt ID: Q8NC56) using ChimeraX [63].

To calculate the total protein mass at the nuclear envelope and their domain distribution, the repertoire of protein members of the inner nuclear membrane were first listed. Using OpenCell [64], UniProt and AlphaFold, the copy numbers and domain assignments of the proteins were curated. In brief, for each protein, the corresponding AlphaFold structure was examined and structured and disordered domains were annotated manually. The data was further analysed to categorize residues belonging to structured or disordered domains of BAF-LEM proteins, Lamins and the rest (Supplementary Table 1). The tabulated results were then plotted as a pie chart in Extended Data Fig. 1b.

B. Purification of LEM2 proteins

1. LEM2

LEM2 was purified according to the published protocol[7] adapted to in-house equipment. All steps were carried out at room temperature unless otherwise noted. The plasmid encoding LEM2 (a gift from the Frost lab) was inserted into BL21 T7 Express pRare bacterial cells (produced in house) and expanded into 3 L of culture in TB with Kanamycin. Harvested cells were resuspended in lysis buffer (30 mM HEPES pH 7.4, 500 mM KCl, 5% glycerol, 20 mM imidazole, pH 8.0, Benzonase (250 U/mL stock,1:10000 dilution in final volume), 1 mM MgCl2, PMSF (100 mM stock,1:100 dilution in final volume) and cOmplete EDTA-free protease inhibitor cocktail (Roche, #38249996990, 1 tablet/50 mL), and lysed by three rounds of high-pressure homogenization. Lysate was then clarified by centrifugation (30,000g, 30 min), loaded on a pre-equilibrated PureCube 100 Compact Cartridge Ni-INDIGO column (Cube Biotech, #75302, 5 mL column volume, 5 mL/min loading rate, room temperature), and washed extensively with

lysis buffer. Protein was eluted with lysis buffer supplemented with 300 mM imidazole, pH 8.0. The imidazole eluate was diluted using ice-cold shock buffer (40 mM HEPES pH 7.4, 5% glycerol) to bring down the salt concentration to 50 mM to induce the phase separation of His_6-SUMO-LEM2. After incubation in ice for 20 minutes, the droplets were pelleted by centrifugation (10,000g, 10 min, 4 ºC). The pellet was resuspended in 5 mL high-salt buffer (40 mM HEPES pH 7.4, 500 mM KCl, 5% glycerol) to dissolve the droplets. To this mixture, His6-Ulp1 (3.2 mg/mL stock, 1:500 equivalents) was added (4 ºC, overnight) to induce the cleavage of His6-SUMO tag. Spin-concentrated cleaved protein was further purified by size exclusion chromatography using the HiLoad Superdex 200 pg 16/600 column in high salt buffer. The LEM2-containing elution fractions were pooled, concentrated, and snap frozen in liquid N_2 as single-use aliquots.

2. $LEM2_{MUT}$

$LEM2_{MUT}$ (Extended Data Fig. 1f) was purified following the LEM2 protocol, with the following modifications: the lysis buffer contained 350 mM KCl instead of 500 mM, the storage buffer had 110 mM KCl instead of 350 mM, and the preparatory phase separation step was omitted.

C. Purification of BAF

Full-length human BAF (Uniprot ID O75531) was purified following published protocols [9,61] with modifications to in-house equipment. His_6-SUMO-BAF was cleaved using His_6-Ulp1 protease (30 min, room temperature) to generate traceless BAF. The protein was then purified via a Superdex 200 pg 16/600 gel filtration column, and fractions containing the BAF dimer were pooled, concentrated, flash-frozen in liquid nitrogen, and stored as single-use aliquots at -80 °C.

D. Protein labelling for fluorescence imaging

LEM2 was fluorescently labeled using DyLight 650 NHS Ester (Thermo Fisher, #62265). For imaging, 1% labeled protein was mixed with the unlabeled fraction. BAF was labeled with DyLight 488 NHS Ester (Thermo Fisher, #46402), with a 5% labeled fraction supplemented for imaging experiments. The labeling efficiency was calculated from the UV-Vis spectrum of the labeled protein according to the manufacturer's instructions (Extended Data Fig. 4j).

Section 2: Preparation of DNAs used in optical tweezer

A. λ-DNA

Commercially available biotinylated bacteriophage λ-DNA was bought from Lumicks (#SKU: 00001) which has 6 biotins on the 3' end of one strand and 4 biotins on the 3' end of the other strand. In case of protein counting calibration measurement, described later, biotinylated λ-DNA with 2x ATTO 647N was used, also bought from Lumicks (#SKU: 00020).

B. NPS DNA

Two repeats of a 172 bp sequence, each containing a 147 bp nucleosome positioning site (NPS)
(ACAGGATGTATATATCTGACACGTGCCTGGAGACTAGGGAGTAATCCCCTTG
GCGGTTAAAACGCGGGGGACAGCGCGTACGTGCGTTTAAGCGGTGCTAGA
GCTGTCTACGACCAATTGAGCGGCCTCGGCACCGGGATTCTCCAG
and a 25 bp spacer (GGCGGCCACGAGATCCAATACATGC) were cloned into the pET-28a vector and amplified to 12 repeats using a previously described method [65]. The 12 NPS-spacer sequences, along with an additional 25 bp spacer and 57 bp flanking sequences, were excised from pET-28a and inserted into the 18,397 bp plasmid TH1704 via *XhoI/NcoI* restriction sites, generating the 19,887 bp plasmid TH1704-12NPS. This plasmid was linearized alongside the 23,286 bp fosmid TH1703 using *BamHI* and *HindIII*, followed by ligation to form the 39,782 bp fosmid TH1703/04-12NPS, with the 12 NPS repeats centrally positioned within a *NotI*-linearized plasmid. For optical tweezers experiments, *NotI* overhangs were ligated to biotinylated handles following [65,66] . A 1,870 bp DNA segment from pET-28a, containing a *PspOMI* site near the center (1 bp offset), was PCR-amplified (primers: CGAGATCTCGATCCTCTACG, GCTAACCAGTAAGGCAACC) in the presence of 10% Biotin-16-dUTP. Digestion with *PspOMI* produced *NotI*-compatible overhangs, generating randomly biotinylated 932 bp and 934 bp handles, which were ligated to the ends of the *NotI*-linearized 39,782 bp fosmid TH1703/04-12NPS. GC content of the DNAs were calculated as a moving average of counts of G and C with a window size 1000 base pairs in Extended Data Fig. 2a-b.

Section 3: Bulk Assays

A. Fluorescence microscopy of phase separation and co-condensation

Fluorescently labelled LEM2, BAF and DNA oligos were assayed for phase separation (Extended Data Fig. 1k-l) and co-condensation (Fig. 1b, with FUS in Fig. 1m, Extended Data Fig. 1g) by spinning disc confocal microscopy, performed in glass-bottom ULA coated low-binding 384-well plates (Revvity #6057302). Reaction was assembled directly in the 384 well plates with a total system volume of 20 µL. The phase separation of LEM2 was triggered by diluting the protein in a working buffer (30 mM Hepes pH 7.4, 150 mM KCl) to bring down the salt concentration from 500 mM KCl in the storage buffer to 150 mM KCl. A concentration titration was performed to screen for phase separation across concentrations (Extended Data Fig. 1l). The formed LEM2 droplets were allowed to grow and settle for 30 min before the start of confocal imaging. The droplets were imaged with an Andor Eclipse Ti inverted spinning-disc microscope with an Andor iXon 897 electron-multiplying charge-coupled device camera and Yokogawa CSU-X1 disc (10000 rpm). The droplets were imaged using either a UPLSAPO ×100/1.45 numerical aperture (NA) oil-immersion objective or ×60/1.20 NA water-immersion objective (Nikon).

For co-condensation assays, different components were assembled together. LEM2 was diluted to 5 µM final concentration and 150 mM salt concentration to allow droplet formation alongside BAF and DNA-oligos. After 30 min of incubation at room temperature, the co-condensates were imaged to examine enrichment or exclusion of individual components. For multichannel imaging, LEM_{NTD} was labeled with DyLight 650, BAF was labeled with DyLight 488 and DNA-oligo was labeled with Atto 565. FUS was tagged with eGFP. Excitation wavelengths were: 488 nm for DyLight 488; 561 nm for Atto565; 640 nm for DyLight 650.

B. Concentration titration for C_{sat}

For concentration titration (Extended Data Fig. 1k-l) of LEM2 in order to measure C_{sat} , LEM2 dilutions of different concentrations were assembled in a water-in-oil emulsion, imaged and analysed as described in the in-house developed inPhase method for identifying phase diagrams [33].

C. FRAP of condensates to measure recovery timescales

LEM2 droplets with 1% labeled fraction were assembled in glass-bottom ULA-coated 384-well plates (PerkinElmer) and allowed to grow for 0.5 hr, 1 hr, 2

hr, 2.5 hr, and 3 hr. FRAP and droplet dynamics were imaged (Extended Data Fig. 3c) using an Andor Eclipse Ti inverted spinning-disc microscope with an Andor iXon 897 EMCCD camera, Yokogawa CSU-X1 scan head (10,000 rpm), and FRAPPA unit. A UPLSAPO ×100/1.45 NA oil-immersion objective (Nikon) was used, with 650 nm excitation for DyLight 650. Photobleaching was done with a 638-nm laser at 70% power for 20 ms per bleaching event. Images were captured pre-bleach (2 frames, 10 ms interval) and post-bleach (91 frames, 10 sec interval). The bleached spot and background were identified manually, and mean intensities were recorded using FIJI. Further data analysis was carried out using a custom MATLAB script to account for natural photobleaching, data normalization to pre-bleach condensate intensity and to determine the recovery timescales from a simple exponential fit for each condensate of different age. Replicates were aligned to the time of bleaching, averaged, and plotted mean ± s.d in Extended Data Fig. 3c,d.

Section 4: Optical tweezers

A. Protein Binding Kinetics on stretched DNA:

Optical tweezer experiments were performed using a C-Trap system (LUMICKS) with a microfluidic flowcell containing separate laminar flow channels. Two streptavidin-coated polystyrene beads (~4.34 µm, Spherotech #SVP-40-5) were trapped and moved into a channel with biotinylated DNA (λ-phage or custom made NPS DNA; 10 ng/ml; Extended Data Fig. 2a,b) in a working buffer (20 mM HEPES, 150 mM KCl, pH 7.5). Single DNA tethering was confirmed by monitoring inter-bead distance and tension during modulation of the “steerable trap,” ensuring the resulting tension-distance curve matched the eWLC model. Following tether confirmation, either a constant trap position or constant tension protocol was used based on experimental requirements.

1. Constant trap position protocol:

In this case, beads tethered with DNA were first moved into a working buffer channel, where optical trap positions were fixed to apply a tension of ~40 pN. Without altering trap positions, the bead-DNA assembly was transferred to a channel containing various protein combinations in the same buffer. Depending on the proteins, incubation lasted several tens of seconds to allow binding (Fig. 1d). Real-time binding was monitored using integrated confocal imaging. As a control, the labeling dye alone showed no DNA association (Extended Data Fig. 2c). Tension was continuously

recorded to assess whether protein binding altered DNA mechanics. Trap positions remained fixed throughout and maintained to a position that resulted in ~40 pN tension on naked DNA. Binding was observed for ~100 s (BAF-LEM2) or ~40 s (BAF, BAF-LEM2$_{MUT}$). Tension increase (ΔT, Fig. 2b) was calculated as the difference between the mean tension during the final ~5 s in the protein and buffer channels.

To assess the impact of tension and protein concentrations on binding kinetics (Fig. 2c), the same protocol was repeated with trap separations adjusted to apply ~30 pN or ~20 pN at different LEM2 concentration (with BAF:100nM).

2. **Constant tension protocol :**

To investigate how protein binding affects DNA stiffness, tethered DNA was first transferred to a working buffer channel, where a constant tension was applied using a PID-enabled force-feedback system integrated with an optical tweezer setup. Maintaining this constant tension, the bead-DNA assembly was then moved to a channel containing various protein combinations and the binding was monitored via confocal imaging. The binding of the BAF-LEM2 module to DNA increased its stiffness, as indicated by a reduction in end-to-end distance (Extended Data Fig. 4c,e).

B. Observation of DNA-BAF-LEM2 co-condensates:

After proteins bound to stretched DNA, co-condensates formed as slack was introduced by stepwise reduction of the DNA end-to-end distance to ~5 µm. At each step, the steerable trap was moved ~800 nm toward the fixed trap, allowing the system to reach steady state while recording tension and end-to-end distance (Extended Data Fig. 2j for BAF; Extended Data Fig. 2l for BAF-LEM2). Tension required finite time to equilibrate (Extended Data Fig. 2k, m), with equilibration time depending on protein combination and concentration. Steady state was typically reached within ~50 s, during which trap positions remained fixed. One mean steady-state tension-distance curve (red curve in Extended Data Fig. 2j,l) was generated by averaging tension and end-to-end distance over the final 5 s of each step. The average steady-state tension as a function of end-to-end distance for each protein condition (Fig. 1e, Extended Data Fig. 2f) was obtained by averaging multiple steady-state traces, binned by end-to-end distance (bin size ~650 nm). Notably, quantification of average tension in the co-condensate regime

across different BAF concentrations shows that DNA binding by BAF saturates at around 100 nM (Extended Data Fig. 2f,g).

C. Co-condensed energy calculation :

The co-condensation energy per DNA base pair was calculated by first determining the total length of condensed DNA. At each end-to-end distance (d_i) and corresponding tension (T_i), the contour length of "non-condensed" DNA ($L_{nc,i}$) was computed using the eWLC model (black dashed line, Extended Data Fig. 2j, 2l):

$$L_{nc,i} = d_i/(1 - \frac{1}{2}\sqrt{\frac{k_B T}{T_i P}} + \frac{T_i}{S})$$

where *P* is the persistence length (~50 nm) and *S* is the stretch modulus (~1300 pN for BAF; ~2000 pN for BAF-LEM2). The "co-condensed length" was then $L_{c,i} = L_0 - L_{nc,i}$, with L_0 ~16.5 µm for λ-DNA (Extended Data Fig. 2n). The co-condensation energy per base pair was obtained by calculating the area between the tension-distance curves of naked and protein-bound DNA, normalized by ($L_{c,i}$/0.34), using 1bp=0.34nm.

D. FRAP of co-condensates in optical tweezer:

Fluorescence recovery after photobleaching (FRAP) was performed by first acquiring a ~5 s time series of confocal images of the co-condensate using low laser excitation (10%). A region of interest (ROI) that included one or more condensates was then photobleached using high laser excitation (90%) for 1s. Recovery was monitored by capturing a long time series (~100 s) at low laser excitation (10%) to track fluorescence recovery (Extended Data Fig. 2i).

E. DNA-co-condensate disassembly experiment :

After co-condensates were formed due to slack, the DNA was gradually stretched by moving one trapped bead with the steerable trap while recording tension. Confocal imaging was used throughout to capture condensate dynamics under applied tension. Pulling was performed at two speeds (10 nm/s and 250 nm/s), with no significant difference in dissembling behavior (Extended Data Fig. 3a). The average tension-distance curve (Fig. 1i) was generated by binning data by end-to-end distance (~250 nm bins) and calculating the mean tension for each bin.

To assess the temporal stability of co-condensates (Extended Data Fig. 3b), the trap-to-trap distance was abruptly increased from 5 µm to 10 µm and held for ~10 min. This induced a rapid tension spike (~80 pN for BAF-LEM2; ~40 pN for BAF), followed by a gradual decline to a stable value above the co-condensate plateau. This slow decrease suggests a delayed disassembly of DNA from the condensates, indicative of a long relaxation timescale and a potential hardening effect.

F. Co-condensates disassembly work calculation :

The amount of DNA within co-condensates ($L_{c,i}$) during unraveling (Fig. 1j) was determined using previously described eWLC-based calculations from the tension (F_i) and corresponding end-to-end distance (d_i) in the mean tension-distance traces (Fig. 1i). For BAF-LEM2, F_i was set to 65 pN to determine d_i. This d_i was then used to find the corresponding tension in the BAF condition and hence corresponding co-condensed length. The total co-condensed DNA length (L_T) at 5 µm end-to-end distance was set as the reference point (100% wrapped). The amount of DNA unraveled at each step was computed as $L_T-(L_0-L_{c,i})$. The disassembly work per base pair was calculated by integrating the area between the tension-distance curves of protein-bound and naked DNA, then normalizing by the amount of DNA base pairs unraveled till 65pN.

G. DNA stretching experiment without co-condensates :

Proteins were first allowed to bind to DNA held in an extended state for ~100 s under tension ≥20 pN using constant tension mode, as previously described - a condition that prevented co-condensate formation. Following binding, the tethered DNA was continuously stretched at 250 nm/s by moving the steerable trap, and the extension continued until the tether ruptured (Fig. 2d, Extended Data Fig. 4b).

H. Calculation of DNA rest length :

Rest length was estimated from an asymptotic fit to the eWLC model, ($T = S(d-L_0)/L_0$), which fits well at high tensions (T~1000 pN) and yields a rest length equal to the contour length (~16.5 µm for λ-DNA, Extended Data Fig. 4a). Due to experimental limitations, a linear fit between 25-50 pN to the eWLC model (P = 50 nm, S = 1300 pN) was used as an approximation, yielding a lower rest length via the x-intercept calculation. This was consistent with rest length estimates

obtained from (i) linear fitting of final end-to-end distances in constant tension mode, yielding ~15.81 ±0.08 μm (Extended Data Fig. 4c), and (ii) linear fitting of the average traces from DNA stretching experiments without co-condensates, yielding ~15.84±0.02 μm (Fig. 2d). DNA stretching experiments with NPS DNA (Extended Data Fig. 4b) showed the same result: the rest length was ~12.90±0.07 μm for naked DNA and ~12.93±0.04 μm with BAF-LEM2 module.

I. Calculation of DNA stiffness :

DNA stiffness at a given BAF-LEM2 concentration was determined using two complementary methods: (i) from the slope of a linear fit to DNA stretching traces in the absence of co-condensates (Fig. 2d, protocol described above), and (ii) from the slope of a linear fit to final end-to-end distances measured at varying tensions using the constant tension method (Extended Data Fig. 4c, protocol described above). Fig. 2e shows the effective DNA stiffness obtained via the second method, plotted as a function of BAF-LEM2 concentration and fitted using a three-parameter model (SI, Eq. S18). The resulting fit yielded the following parameter estimates with confidence intervals : k_0/N = 50.21 pN [49.05, 51.37], k_i/k_0 = 0.30 [0.26, 0.35], $\exp(\beta\epsilon)c_0/c_L$ = 66.87 [32.69, 101.06].

A control experiment confirmed that stiffness change or tension rise was not due to varying LEM2 binding to DNA at different tensions, as average bound fluorophore intensity (tagged to LEM2) remained constant across tensions (Extended Data Fig. 4m).

J. Analysis of LEM2/SO intensity distribution along DNA length:

To correct for background protein (LEM2 or SO) signal, a small ROI excluding DNA and beads was selected from the confocal image (cyan box, Extended Data Fig. 4k). The mean intensity (b^k) due to protein of choice (k = LEM2 or SO) of this ROI was subtracted from each pixel intensity, $I^k_{i,j}$, of the image, where i and j denote row and column indices of the pixel considered. The protein intensity along DNA was calculated as a function of column index j :

$$I^k_j = \sum_{i=1}^{N_1} (I^k_{i,j} - b^k)$$

with N_1 representing the number of rows in the considered ROI of the image. Finally the protein intensity was normalised by the maximum intensity as $I^k_{norm,j} = I^k_j / max(I^k_j)$ (Fig. 1l, Extended Data Fig. 3g). Pearson correlation coefficient between the LEM2 and SO signal was calculated as

$$Pearson\ correlation\ coefficient = \frac{\sum_{j=1}^{N_2}(I_{norm,j}^{LEM2} - <I_{norm,j}^{LEM2}>)(I_{norm,j}^{SO} - <I_{norm,j}^{SO}>)}{\sqrt{\sum_{j=1}^{N_2}(I_{norm,j}^{LEM2} - <I_{norm,j}^{LEM2}>)^2}\sqrt{\sum_{j=1}^{N_2}(I_{norm,j}^{SO} - <I_{norm,j}^{SO}>)^2}}$$

where N_2 represents the number of columns in ROI considered in the image (Extended Data Fig. 3h).

K. DNA stretching experiment with co-condensates in presence SO :

Co-condensates were initially formed by incubating pre-slacked DNA with BAF (100nM) and LEM2 (500nM), along with SO (25nM). Following the previously described protocol, the steerable optical trap was used to stretch the DNA-co-condensate assembly while simultaneously recording the applied tension and imaging the unraveling process. The intensity profiles of LEM2 and SO along the DNA were then quantified using the method described above (Extended Data Fig. 3g). We observe an anti-correlation between LEM2 co-condensates and the SO signal, indicating that DNA tension is high whenever the DNA is outside the co-condensate, and lower inside (Extended Data Fig. 3h). This result is not due to SO exclusion from co-condensates, which is supported by two control experiments revealing a positive correlation between LEM2 co-condensates and SO signal at low tensions that lie within the constant tension plateau (Extended Data Fig. 3g, bottom).

L. DNA overstretching experiment with in presence FUS :

To confirm that FUS binds exclusively to single-stranded DNA (ssDNA), two control experiments were conducted :

1. NPS-DNA stretching in the presence of FUS:

An NPS-DNA construct stretched with 200 nM GFP-FUS (in working buffer, described previously) showed binding only above ~80 pN (Extended Data Fig. 3i,j), to the melted ssDNA. No binding occurred below 65 pN, consistent with previous reports where biotinylated, bead-tethered strands prevented peeling under high tension (Extended Data Fig. 2b).

2. λ-DNA Overstretching and Exposure to BAF + LEM2 + FUS:

λ-DNA was overstretched and partially melted at ~65 pN due to the presence of nicks. Upon exposure to a mixture of BAF-LEM2 and FUS,

complementary binding of FUS to ssDNA and BAF-LEM2 to dsDNA was observed (Extended Data Fig. 3k). No binding of FUS to dsDNA was detected under the working buffer conditions.

M. Protein count on DNA :

To avoid nonspecific signal from proteins bound to the beads, the number of proteins bound to DNA was quantified within a ROI (Extended Data Fig. 4k) carefully selected to exclude the beads. The total number of DNA-bound proteins was then extrapolated from this ROI.

To estimate the number of proteins bound to stretched DNA in the optical tweezer setup, the confocal volume, V_C, of the imaging system was determined by imaging λ-DNA labeled with ATTO-647N (Lumicks, #SKU: 00020) across different focal planes (z-stacks). Extended Data Fig. 4g shows the total photon count from an individual fluorophore as a function of z-position, with *z=0* corresponding to the plane of maximum intensity. The data were fitted with a Gaussian to determine the full width at half maximum (FWHM), giving the confocal depth (~Δz). Photon count distributions along the x and y directions at z = 0 (Extended Data Fig. 4h,i) were fitted with Gaussians to extract the FWHM, representing the point spread function in x and y (Δx, Δy). The confocal volume was then calculated as $V_C = \Delta x \cdot \Delta y \cdot \Delta z$.

In point-scanning mode, the background intensity per pixel in DNA-free regions corresponds to fluorescence from a single confocal volume, representing $c \cdot V_C$ LEM2 molecules, where *c* is the LEM2 concentration (Extended Data Fig. 4k). The average intensity per protein molecule was then estimated as $I_p = b^{LEM2}/(c \cdot V_C)$ where b^{LEM2} is the average background photon count per pixel in bulk, calculated from a small ROI excluding DNA and beads. The total background-subtracted photon count in the ROI, which includes the DNA, was computed as $J = \sum_{j=1}^{N_2} \sum_{i=1}^{N_1} (I_{i,j}^{LEM2} - b^{LEM2})$ where N_1 and N_2 are the total number of rows and columns in the ROI. The number of bound LEM2 (Extended Data Fig. 4l) was then calculated as $J * (d/0.08)/(N_1 * I_p * f_{eff})$, where *d* is the DNA end-to-end distance (in μm), 0.08 μm is the pixel size, and f_{eff} (= 66%, Extended Data Fig. 4j, methods) is the fluorescence labeling efficiency, representing the fraction of labeled versus total LEM2 molecules.

Section 5: Cell biology, Imaging and Analysis

A. Cell lines and cell culture

All cell lines used in this study were routinely tested and confirmed negative for mycoplasma contamination. Their sources and authentication details are provided in the SI. Cells were cultured in McCoy's 5A medium (Gibco, #16600082) with 5% (v/v) fetal bovine serum (FBS; Gibco, #A5670701) and, when overexpression constructs were used, supplemented with puromycin (0.5 µg/mL, Gibco, #A11138).

Cells were cultured in T25 or 60 mm plastic dishes or 35 mm glass-bottom dishes (Nunc, #169900, 150288 & 150680 respectively) or 8-well glass-bottom µ-slides (Ibidi, #80827). Cells were regularly inspected for growth and passage using a Nikon Eclipse TS2 cell culture microscope with 10X or 40X air objective. Cells were counted either manually using a Neubauer chamber or using Luna II brightfield cell counter. Cells were always maintained at 37 °C and 5% CO_2 while storing and imaging. LEM2, BAF, and Lamin A/C were visualized via stable expression of C-terminal mNeonGreen-tagged constructs. Live-cell imaging was performed in McCoy's 5A medium with 5% (v/v) FBS, omitting phenol red to minimize autofluorescence.

B. CRISPR/Cas9-mediated generation of HCT116 knock-in lines

Cell lines that stably express fluorescently labelled marker proteins, BAF-mNeonGreen, LEM2-mNeonGreen and Lamin A/C-mNeonGreen were produced by the Genome Engineering Facility at MPI of Molecular Cell Biology and Genetics, Dresden. Genome editing was performed using a CRISPR–Cas9 nickase strategy.

hBAF and hLEM2 were targeted for C-terminal tagging, hLamin A/C for N-terminal tagging with mNeonGreen in HCT116 cells (Public Health England #91091005). Sequences of target regions were analyzed for appropriate guide RNA binding sites using the Geneious (2022.1.1, http://www.geneious.com/) software and the CRISPOR design webtool (http://crispor.tefor.net/). The genomic target sequences in HCT116 cells were checked beforehand for a perfect match with sequences of guide RNAs and targeting constructs by Sanger sequencing. Guide RNAs (SI) were ordered as crRNA from IDT (Integrated DNA Technologies). crRNAs were duplexed with tracrRNA (IDT #1072534) by mixing equimolar amounts. Targeting constructs containing codon-optimized mNeonGreen flanked by 500 bp homology arms were generated through Gene Synthesis by Genscript (sequences in SI). HCT116 cells were transfected with

RNP (44 pmol cr:tracr duplexes and 37 pmol Cas9, IDT #1081061) and 500 ng of targeting construct using the NEON transfection system (1530V, 20ms, 1 pulse). 72 h post-electroporation single-cell sorting was performed in a BD FACSAria Fusion flow cytometer (Beckton Dickinson). Genomic DNA from single-cell clones was extracted using the QuickExtract DNA extraction kit (Epicentre) following the manufacturer's instructions. Cell clones with tagged allele (BAF: monoallelic, Lamin A/C: biallelic and LEM2: biallelic) were identified by PCR using Phusion Flash High-Fidelity PCR Master Mix (ThermoFisher) and verified by Sanger Sequencing (primer sequences in SI).

C. Plasmid and small interfering RNA transfections

For both transient and stable expression of fluorescently labelled markers, we used pMGF196 vectors having siRNA resistant gene for protein or mutant of interest coupled with an antibiotic resistance gene for puromycin that allow the protein of interest and the resistance gene to be expressed from the same transcript. The plasmids encoding LEM2-mCherry and $LEM2_{M21}$-mCherry were a gift from the lab of Katie Ullman, University of Utah. The blotted plasmids were extracted into solution and midi-prepped for further use. The plasmid encoding mApple-53BP1trunc was purchased from Addgene (#69531).The plasmid encoding $LEM2_{MUT}$-mCherry was prepared by Gibson assembly of human codon-optimised synthesised $LEM2_{MUT}$ gene block and pMGF196 backbone coding for mCherry and puromycin.

For transient expression, plasmids were transfected using X-tremeGENE 9 DNA transfection reagent (Roche, #XTG9-RO) or Lipofectamine 2000 (Invitrogen, #11668019) following the manufacturer's instructions. Transfected DNA amounts were optimized for each assay and varied between 5 µg and 8 µg per 20 µl transfection reagent in 250 µl Opti-MEM (Gibco, #11058021). After adding the plasmid-lipid mix, the cells were incubated for 24 h before replenishing fresh medium (imaging medium for direct confocal imaging, or McCoy's 5A with 5% FBS supplemented with 5 µg/mL Puromycin for antibiotic selection, accordingly). For stable expression, plasmids were transfected using Lipofectamine 2000, and incubated for 24 h before antibiotic selection.

Small interfering RNAs (siRNAs) targeting BAF or LEM2 were obtained from previous studies[8,9]. siRNAs were delivered with lipofectamine RNAiMax (Invitrogen, #13778150) according to the manufacturer's instructions. BAF (also known as BANF1) was targeted using 10 nM s16808 (AACGGAUUGAAAGUGAGGGtt), IDT, including a 3′ overhanging tt dinucleotide

for increased efficiency) and analysed after 48 h; LEM2 was targeted using 10 nM (UACAUAUGGAUAGCGCUCCtt, IDT, including a 3′ overhanging tt dinucleotide for increased efficiency) and analysed after 48 h. A scrambled siRNA sequence (UCUACGAUCGGAGAUUUGCtt, IDT, including a 3′ overhanging tt dinucleotide for increased efficiency) was used as a non-targeting siRNA control.

D. Western blotting

HCT116 Lamin A/C-mNeonGreen cells treated with siLEM2 or siCtrl were scratched from the culture dish and lysed in disruption buffer (NP40 Lysis buffer, #J60766.AP, 50mM Tris-HCl (pH 7.4), 150mM NaCl, 1% NP-40 and 5mM EDTA). The soluble protein fraction was separated by centrifugation (30 min, 30,000 xg), and the supernatant was collected. Total protein concentration was measured using a Bradford assay. Optimized amounts of lysate (10 or 25µg) from both control and knockdown samples were loaded on NuPage 4–12% gradient Bis–Tris gels (Invitrogen, #NP0321BOX) and transferred to a nitrocellulose membrane (Bio-Rad, #1620112) via wet blotting. LEM2 was detected with a polyclonal rabbit anti-LEM2 antibody (Sigma Aldrich, HPA017340, 1:500), and GAPDH was used as a loading control, probed with a polyclonal mouse anti-GAPDH antibody (Invitrogen, MA5-15738, 1:5000). The membrane was imaged (Extended Data Fig. 7e) using the iBright Gel Documentation System (Thermo Fisher Scientific) and analyzed in FIJI.

E. Cell compression assays

Cells to be compressed were seeded on fibronectin (Gibco, #33016015) coated (2 h) coverslips (12 mm × 12 mm) at a density of 0.8×10^5 cells/mL in 30 mm dishes and incubated at 37°C with 5% CO_2 for two days. On the third day, cells were washed three times with PBS (3 mL each) before aspirating excess liquid to ensure a dry surface. A 100 µL medium droplet containing spacer beads (3 µm or 6 µm, diluted 1:1000 from a 2.5% w/v stock, Polysciences Polybead® microspheres, Cat: 17134-15 (3 µm) and 07312-5 (6 µm)) was added to the coverslip to form a dome. After 5 min of bead settling, a clean coverslip was placed on top, gently touching one edge before release. The medium was blotted away using Whatman filter paper until the coverslips were nearly in contact, compressing the cells for 5 min. Fresh medium (3 mL) was then flushed into the dish to allow the top coverslip to float before removal. Cells were incubated for 30 min post-compression before proceeding with immunofluorescence staining. The compression of cells was verified by visualizing the disruption of microtubule organisation in immunostaining for tubulin (Synaptic Systems, #302 206G) in Extended Data Fig. 9a.

For cell compression with real-time imaging, the same protocol was followed, except that cells were seeded on 30 mm glass-bottom dishes, and circular coverslips were used to compress the cells from above.

F. Live-cell microscopy

Confocal microscopy to test stable expression of endogenously mNeonGreen tagged LEM2, BAF and Lamin A/C was performed on Andor Olympus IX81 inverted spinning disc confocal microscope equipped with Andor iXon 897 EMCCD camera, Yokogawa CSU-X1 (5000 rpm, pinhole diameter 50 µm, pinhole spacing 250 µm) and with temperature, O_2, and CO_2 control. The excitation wavelengths were 405 nm, 488 nm, 561 nm and 640 nm. The images were acquired using either an Olympus U Plan SApo 60X (1.35 NA) Oil-immersion or Olympus U Plan SApo 100X (1.4 NA) Oil-immersion objective. The microscope was controlled using Andor iQ 3.6 software with custom made protocols.

Cells with siRNA treatments (Extended Data Fig. 7a,c), transient or stable expression of fluorescently tagged proteins and BAF-mNeonGreen cells for measuring BAF distribution were imaged using an Andor Revolution spinning disk confocal system on an Olympus IX83 inverted microscope with a cage incubator for temperature, CO_2, and O_2 control. Excitation was provided by 405 nm, 445 nm, 488 nm, 514 nm, 561 nm, 633 nm, and 726 nm lasers from two Andor ILE units. A Yokogawa CSU-W1 (4000 rpm) spinning disk unit with 50 µm pinhole (500 µm spacing) was used. Images were acquired with an Andor iXon 888 Ultra EMCCD camera using either an Olympus UPlanSApo 100X (1.4 NA) oil-immersion or Olympus U ApoN 150X (1.45 NA) objective. The system was controlled with Andor iQ 3.6 software with custom made protocols.

Imaging for nuclear shape analysis across knockdowns and imaging of cells with live-cell compression were performed using an Olympus IXplore SpinSR spinning disk confocal system on an Olympus IX83 inverted motorized stand with hardware autofocus (ZDC2) and a stage-top Z-piezo (400 µm range). A cage incubator maintained temperature, CO_2, and O_2 levels. Excitation was provided by 405 nm, 445 nm, 488 nm, 515 nm, 561 nm, and 640 nm lasers. A Yokogawa CSU-W1 (4000 rpm) spinning disk unit with 50 µm and SORA disks enabled standard and super-resolution imaging. Images were acquired with two Hamamatsu ORCA-Fusion BT Digital CMOS cameras using Olympus UPlanSApo 10X (0.4 NA) air or Olympus U-ApoN 100X (1.49 NA) oil-immersion

objectives. The system was controlled with Olympus cellSens 4.1 software with custom made protocols.

G. Immunofluorescence

Immunofluorescence (IF) was performed at room temperature unless stated otherwise. Cells were either compressed (as mentioned before) or left uncompressed and proceeded to wash. The medium was aspirated out and washed gently with PBS twice. The cells were then fixed in 2% paraformaldehyde (10 min, dark, Thermo Scientific Chemicals, 043368.9M, diluted using PBS) and permeabilized with 0.2% Triton-X 100 (5 min, dark, Thermo Scientific Chemicals, #J66624.AP). Blocking was done using PBS-Tween-BSA (30–40 min, dark, Thermo Scientific Chemicals, #003005). Primary antibodies were diluted in PBS-Tween-BSA (50 µL per coverslip) and incubated in a humidity chamber for 1 hour at room temperature or overnight at 4°C. Coverslips were washed twice with PBS before secondary antibody staining (1:1000 in PBS-Tween-BSA, 30 min–1 hour, dark). DAPI/Hoechst (1:10,000, Invitrogen, #62248 or H21492) was added in the final PBS wash (10 min, if required). Coverslips were mounted using Vectashield (5 µL per coverslip, Vectorlabs, #H-1000-10) and sealed with nail polish. Samples were imaged within one week to prevent signal decay.

Primary antibodies used for immunodetection included polyclonal rabbit anti-LEM2 (Sigma Aldrich, #HPA017340), chicken anti-tubulin (Synaptic Systems, #302 206G), rabbit anti-BANF1 (Abcam, #AB129184), mouse anti-53BP1 (Merck Millipore, #MAB3802) and mouse anti-cGAS (Cell Signalling, #15102T). Fluorescently labeled secondary antibodies (Goat anti-rabbit 488, anti-mouse 488, anti-rabbit 647, and anti-rabbit 568; Invitrogen) were used for detection. The stained samples were imaged by laser-scanning confocal microscopy using a Leica Stellaris 8 Falcon upright microscope with a white light laser that allows excitation of fluorochromes at any wavelength in a range of 440 - 790 nm and a 405 nm DMOD diode laser. The microscope is equipped with an 8 kHz tandem scanner. Detection was achieved using three Power HyD S, one Power HyD X, and one Power HyD R detectors, along with a Hamamatsu Flash 4.0 V3 camera. Images were acquired using an HC PL APO 63X (1.40 NA) oil-immersion objective or HC PL APO 10X (0.30 NA) air objective. The microscope was controlled using Leica LAS X software with custom made protocols.

H. DNA damage and nuclear envelope rupture analysis

Cells (control and knockdown conditions) were compressed (6 μm or 3 μm) as described before. Uncompressed cells were used as control for mechanical strain. DNA damage in interphase cells (with and without compression across knockdowns) was assessed using anti-mouse 647 against mouse anti-53BP1 and anti-chicken 568 against chicken anti-tubulin. Nuclear envelope rupture (with and without compression across knockdowns) was assessed using anti-mouse 647 against mouse anti-cGAS and anti-chicken 568 against chicken anti-tubulin. DNA was stained with DAPI in all the cases (1:10000). LEM2 was imaged using the endogenous mNeonGreen tag. The imaging datasets for DNA damage and cGAS were acquired separately. For each field of view, a complete z-stack covering the whole of nuclei was recorded for all the four channels imaged (405: DAPI, 488: LEM2-mNeonGreen, 561: Tubulin, 647:53BP1). Each condition was imaged in three biological replicates (Fig. 4a, Extended Data Fig. 9c,h).

DNA damage was assessed using a custom ImageJ macro. Maximum intensity z-projections of the DNA and 53BP1 channels were generated. Nuclei masks were created by applying an Otsu threshold to segment nuclei based on DNA intensity contrast. Nuclei touching the image boundaries or exhibiting mitotic or degraded morphology were excluded based on size, circularity, and coordinates. The masks were applied to the 53BP1 channel to restrict damage quantification to nuclear regions and reduce background interference. DNA damage foci, defined as 53BP1 clusters ranging from 5 to 20 pixels, were counted in each nucleus. Given minimal intra-field variation, the number of foci per nucleus was calculated for each field (image positions were randomized). Data from all replicates were pooled and plotted as bar plots displaying mean ± s.d. with individual data points (Fig. 4c, Extended Data Fig. 9d).

Nuclear envelope rupture was evaluated using a similar approach, incorporating the measurement of the total intensity of cGAS at each focus after background subtraction. Data were pooled from three independent replicates for each knockdown and compression condition and analyzed to determine the percentage of cells with cGAS foci (100 × number of cGAS foci per nucleus) and the total cGAS intensity per nucleus in each image. The results are plotted in Extended Data Fig. 9i,j as bar plots displaying the mean ± s.d. with individual data points shown.

I. DNA damage close to nuclear periphery

DNA damage foci near the nuclear periphery were quantified using a custom workflow in Imaris, based on the same immunofluorescence imaging dataset. Using the DNA channel in the 3D volume image, nuclei were reconstructed into 3D surfaces using the Surfaces function with automatic thresholding, and clumped nuclei were separated by applying a seed diameter of 8 μm. Incomplete nuclei or those touching image boundaries were excluded, and additional filtering removed abnormally large or small nuclei (e.g., mitotic or defective). Damage foci were segmented from the 53BP1 channel using the Spots tool with a typical diameter of 1 μm. Using the MATLAB XTension 'Spots close to surface', foci within 1 μm of the nuclear rim were classified as peripheral, while the rest were considered bulk foci (Extended Data Fig. 9e). Data from three biological replicates were pooled, and the fraction of peripheral foci was plotted for each knockdown condition as a bar plot with mean ± s.d. and scatter of individual data points (Extended Data Fig. 9f).

J. Nuclear invaginations analysis

Nuclear invaginations were analyzed using the same datasets acquired for DNA damage analysis. Image analysis was performed using a custom Python script. The DNA channel was first subjected to a maximum z-projection followed by smoothing using Gaussian blur ($\sigma = 1$) and thresholded using Otsu's method to generate a binary mask. The mask was refined by filling holes and applying morphological opening (disk size: 5-pixel diameter) to remove dark spots within bright objects. Nuclei were then segmented using a watershed algorithm, and those with an area outside 5000–20000 square pixels (pixel size = 100 nm)were excluded.

For each selected nucleus, a contour of the nuclear boundary was generated. Curvatures along the contour were measured using a moving window of 100 points and classified into three categories: -1 for curvature ≤ -0.01, 0 for -0.01 < curvature < 0.01, and 1 for curvature ≥ 0.01. To minimize noise, the curvature profile was smoothed using a 30-point window. Invaginations were identified as regions where the contour exhibited a transition from negative to positive curvature spanning at least 10 pixels (Extended Data Fig. 10a). The number of invaginations per nucleus was calculated for each nucleus in each field of view across replicates. Data were pooled for each knockdown and compression condition and analyzed to generate Extended Data Fig. 10b, where individual points represent replicates, and bars indicate mean ± s.d. of replicate means.

K. Micronucleation under live compression of cells

Cells (control and knockdown conditions) were grown in 30 mm dishes at a density of 8 x 10^5 and proceeded to live cell compression as mentioned before. The cells were pre-incubated with SPYDNA650 (Spirochrome) to stain DNA. The dish containing cells were mounted on a spinning disc confocal microscope within a temperature, CO_2 and O_2 controlled cage as described before. The focus of the microscope was aligned to the midplane of the nuclei of the monolayer of cells by manual inspection. Only one z-plane was imaged given the fast time-scales of compression and subsequent events. 5 frames were recorded prior to compression at an interval of 20 sec and then cells were compressed *in situ*. Imaging was continued immediately after compression recording 91 frames at an interval of 20 sec. Excitation wavelengths were 488 nm (LaminA/C-mNeonGreen) and 640 nm (SPYDNA-650). Representative frames post-compression is shown in Fig. 4b.

Micronuclei in the imaged z-plane were manually counted before and after compression with dataset blinding. Only nuclear fragments with diameters between 1 and 5 μm were classified as micronuclei. The number of new micronucleation events was determined by subtracting the pre-compression count from the post-compression count. Data from different replicates were pooled for each knockdown or compression condition and analyzed to generate Fig. 4d and Extended Data Fig. 10d where mean ± s.d. is displayed as a bar plot with individual data points.

To determine whether live micronuclei budding events are associated with DNA damage, HCT116 cells with endogenously tagged Lamin A/C-mNeonGreen were transfected with a construct expressing mApple-53BP1trunc. Live-cell compression and micronucleation tracking were performed as described, except that 53BP1-trunc was imaged instead of DNA. Due to the low transfection efficiency of the plasmid in these cells, the data were used qualitatively in Extended Data Fig. 10c, without quantitative analysis from live-cell imaging. Instead, fixed compressed samples subjected to immunofluorescence were used for quantification.

L. Counting micronuclei and damage foci inside micronuclei

Micronuclei and DNA damage foci within them were analyzed using a custom CellProfiler pipeline applied to the same immunofluorescence dataset used for DNA damage assessment. First, maximum intensity Z-projections of the DNA

and 53BP1 channels were generated (Extended Data Fig. 10e). The DNA channel was then downsampled (0.5×, nearest neighbor method), followed by morphological opening (disk size = 35 px). The image was upscaled back (2×, nearest neighbor method) and subtracted from the original to have an image with higher contrast between background and foreground (Image #2). To refine segmentation, Image #2 underwent morphological closing (disk size = 13 px), Sobel edge enhancement, and subtraction from the original. Micronuclei were identified using Otsu thresholding (diameter: 10–50 px, form factor ≥ 0.4, area ≥ 50 px²). The resulting mask was applied to the 53BP1 channel, and DNA damage foci were segmented via Otsu thresholding (diameter: 1–15 px, area ≥ 25 px²). Micronuclei counts per nucleus and foci counts per micronucleus were extracted. Data were pooled for each knockdown condition (compressed) and analyzed to generate Extended Data Fig. 10f, where the fraction of nuclei with damaged micronuclei was plotted as mean ± s.d. with individual data points.

M. Imaging and analyzing BAF distribution

The relative abundance of BAF in the nucleus, NE, and cytoplasm was quantified in HCT116 cells endogenously expressing BAF-mNeonGreen. Cells were imaged to track BAF (excitation: 488 nm), DNA (NucBlue, Invitrogen #R37605, excitation: 405 nm), and the plasma membrane (CellMask DeepRed PM stain, excitation: 638 nm). Z-stacks spanning the entire cell volume were acquired for all three channels with a 250 nm step size (Extended Data Fig. 5f).

Image processing and 3D segmentation were performed in Arivis Pro using a custom pipeline. To reduce noise, Gaussian blur ($\sigma = 1$) was applied to the BAF and CellMask channels, while a median filter (3-pixel width) was used for the DNA channel. The nuclear envelope (NE) and cell membrane were detected using the membrane detection tool in Arivis, with thickness and maximum gap size parameters set to 3 and 4 pixels, respectively. Membranes were segmented based on detected contours and Otsu thresholding of BAF and CellMask intensities. A nuclear DNA volume mask was generated via Otsu thresholding of DNA intensity and eroded by 3 pixels to account for confocal resolution limits. The NE volume mask was obtained by subtracting the DNA volume from the total NE-enclosed volume, while the cytoplasmic volume mask was defined by subtracting the NE-enclosed volume from the total cell volume (Extended Data Fig. 5g).

Segmented volumes and corresponding BAF intensity data were exported from Arivis for further analysis. For each nucleus, summed BAF intensities within the cytoplasmic, NE, and nuclear volume masks were computed across five

replicates. Using mean intensity ratios and previously reported total cellular BAF copy numbers from mass spectrometry (OpenCell), the absolute number of BAF molecules per compartment was estimated (Extended Data Fig. 5h).

The mean spacing of BAF dimers on the chromatin surface was calculated using the number of BAF dimers in the NE (N) and the total nuclear surface area (A), following the relation:

$$Mean\ spacing\ (l) = \sqrt{\frac{A}{N}}$$

N. Nuclear envelope enrichment of BAF, LEM2 and DNA

A plasmid encoding LEM2-mCherry was transfected into HCT116 cells, in which BAF was endogenously tagged with mNeonGreen, as described before. After 48 h, the cells were transferred to an imaging medium and stained with SPYDNA-650 for 15 min to label DNA. Imaging was performed using a spinning disk confocal microscope with excitation wavelengths of 488 nm for BAF-mNeonGreen, 561 nm for LEM2-mCherry, and 638 nm for SPYDNA-650. Complete z-stacks spanning the entire nucleus were acquired for all three channels with a z-step size of 250 nm (Fig. 1c, Extended Data Fig. 1i). A custom Python script was used to analyze the images, generating normalized, background-subtracted line intensity profiles across the nucleus for BAF, LEM2, and DNA. The results are presented as mean ± s.d of replicates in Extended Data Fig. 1i.

DNA enrichment at the nuclear rim across knockdowns was assessed using CellProfiler with a custom pipeline. A maximum intensity projection of the DNA channel was performed, followed by Gaussian blur (σ = 1) and segmentation via Otsu's method. The resulting mask was eroded by 5 pixels and subtracted from the original to generate a nuclear envelope (NE) mask. The mean DNA intensity within the NE mask was quantified per nucleus across knockdowns after background subtraction. The corresponding histograms are shown in Extended Data Fig. 1j.

O. Estimating extent of knockdowns of LEM2 and BAF

HCT116 LEM2-mNeonGreen or BAF-mNeonGreen cells treated with control or LEM2 siRNA were transferred to imaging medium after 48 hours and stained with SPY650-DNA for 15 minutes to label DNA. Imaging was performed using a spinning disk confocal microscope, acquiring Z-stacks spanning the entire nucleus (excitation: 488 nm for mNeonGreen-tagged proteins, 638 nm for DNA, Extended Data Fig. 7a,c).

Knockdown efficiency was assessed using a custom Python script based on fluorescence signal loss. Background subtraction was applied to each image, followed by mean intensity projections of the DNA and protein channels. Total protein and DNA intensities were then measured per image. To account for cell number, protein intensity was normalized by dividing it by total DNA intensity. Replicates were pooled, and fluorescence signal loss was quantified as the ratio of mean normalized protein intensity in control versus knockdown conditions. This fraction was converted to a percentage and plotted as bars (mean ± s.d.) with individual data points representing each image (Extended Data Fig. 7b,d).

P. Nuclear surface and shape calculations

For surface reconstruction, siRNA-treated HCT116 LEM2-mNeonGreen cells were used. Following 48 hours of siRNA treatment, cells were transferred to imaging medium, stained with SPYDNA-650 for 15 minutes to label DNA, and imaged using a spinning disk confocal microscope. Excitation wavelengths of 488 nm and 638 nm were used to visualize the mNeonGreen-tagged LEM2 and DNA, respectively, with z-stacks acquired to cover the entire nucleus (step size=250 nm).

Image analysis was performed in Imaris using a custom pipeline. The DNA volume was reconstructed into 3D surfaces using the Surfaces function with automatic thresholding (Fig. 3f). To separate clumped nuclei, a seed diameter of 8 µm was applied. Nuclei that were incomplete in the z-stack or touched image boundaries were excluded, and additional filtering was applied to remove abnormally large or small nuclei (e.g., mitotic or defective). From the reconstructed surfaces, nuclear shape features including total surface area, volume, sphericity, eccentricity, prolate ellipticity, oblate ellipticity, and ellipsoid axis lengths were extracted and exported.

Data from multiple replicates were pooled and analysed using a custom MATLAB script. To calculate nuclear asphericity, the surface area of a sphere with the same volume as the nucleus (A_0) was subtracted from the actual nuclear surface area (A) and the difference was normalized by A_0 for each nuclei.

Histograms of asphericity, sphericity, nuclear volume and surface area across knockdown conditions were plotted (Extended Data Fig. 7j-m). The raw data were fitted to a lognormal distribution using a non-linear least squares method, and key statistical parameters, including mean, median, mode, and peak position, were computed. Sphericities of nuclei were further visualized as nuclear surfaces colored according to a gradient using Imaris (Extended Data Fig. 7i)

The cross-sectional area and circularity of nuclei were quantified from maximum projections of the DNA signal, using a threshold of 137 (range 1–255) for segmentation in Fiji. Area and circularity of segmented particles were directly measured and pooled from three replicates and compared across knockdowns or compression conditions (Extended Data Fig. 7g,h, 9g).

Q. Electron tomography and reconstruction

We used cryo-ET data acquired from FIB milled mouse embryonic stem-cell samples by the Back lab at Max Planck Institute of Biophysics, Frankfurt[43]. Cryo-ET data acquisition and reconstruction were performed by the Beck lab as described [43]. We analysed a total of three tomograms. To enhance the contrast and improve the isotropy, the tomogram was deconvolved, denoised and missing-wedge corrected by the deep-learning based software IsoNet [67]. Segmentation was performed using Dragonfly software (Version 2022.2 for Linux, developed by Object Research Systems (ORS) Inc, Montreal, Canada, 2020; www.theobjects.com/dragonfly)[68]. A small, representative region was selected from the full tomogram, containing key features of interest. Within this area, all voxels were manually segmented and assigned to one of seven classes: membrane, microtubules, nuclear lamina, ribosomes, proteasomes, chromatin, or background. This segmentation was then used to train a neural network. The Deep Learning Tool in Dragonfly was employed to create a multi-slice (five slices) U-Net. The resulting AI segmentations were manually cleaned and refined, with the nuclear lamina requiring a complete manual re-segmentation. Segmentations were exported as binary TIFF images and converted to MRC format using IMOD [69]. Surface smoothing and visualization were done in UCSF ChimeraX 1.8 [63] (Fig. 3a, Extended Data Fig. 5b-d).

The thickness of the hydrogel layer was measured as the distance between inner nuclear membrane and the mass of nucleosomes. The measurements were performed manually in IMOD across different tomogram slices and plotted as a histogram in Extended Data Fig. 5e. The mean thickness of the amorphous layer was calculated from the mean of the fitted normal distribution.

Section 6: AFM on cells: Nuclear stiffness measurements

A. Atomic force microscopy

The nucleus stiffness measurements were performed with a JPK Nanowizard 4XP AFM (Bruker) mounted on an LSM 700 confocal microscope (Zeiss). Can-tilevers with a quadratic pyramidal tip, a half-angle to face of 17.5°, and a nominal spring constant of 0.03 N/m (MLCT-D, Bruker) were used in all experiments. The spring constant was calibrated before each measurement session using the thermal fluctuation method (JPK SPM software, Bruker).

Cells were seeded in glass-bottom petri dishes (Fluorodish, FD35-100) two days before the measurements. One hour before the start of the measurements, the medium was changed to CO_2-independent DMEM (Invitrogen, #12800-017) containing 4 mM NaHCO3, buffered with 20 mM HEPES/NaOH pH 7.2 and supplemented with 10% fetal bovine serum (Life Technologies, #10270106). When latrunculin A (Invitrogen, #L12370) treatment was used, the drug was added to the medium 15 minutes before the start of the measurements to a final concentration of 200 nM. During all the AFM experiments, a petri dish heater (Bruker) was used to maintain the cells at 37°C.

For each measured cell, the nucleus was identified by eye using brightfield or differential interference contrast (DIC) microscopy. A 1 × 1 μm^2 region at the nuclear center was selected using the acquisition software of the atomic force microscope (AFM; JPK SPM, Bruker), and a 3 × 3 grid of measurement points was overlaid. Force mapping was performed in contact mode with a setpoint force of 1 nN and an indentation speed of 1 μm/s, yielding nine indentation curves per cell. For experiments with latrunculin A, a reduced setpoint force of 0.5 nN was used due to increased cell softness. In the LEM2 knockdown condition, confocal microscopy images of mNeonGreen (excitation: 488 nm) were acquired before AFM measurements. Cells in which LEM2-mNeonGreen localized to the nuclear membrane were excluded from indentation, as this indicated incomplete knockdown.

B. Analysis of the AFM data

The indentation curves were first fitted using the AFM manufacturer's software JPK Data Processing (Bruker). In brief, two analysis steps were performed: (i) determining the contact point through Hertz model fitting, and (ii) estimating an apparent Young's modulus through performing a Hertz fit in a defined indentation range of 0.5 μm. A Poisson's ratio of 0.5 was assumed.

In detail, as part of the first analysis step, any tilt or offset in the curve was corrected using the curve's baseline as reference. At this point, curves with no clear baseline were discarded as they denote failed indentation experiments. The Hertz-Sneddon model was then fitted on the part of the indentation curve where the force was below 100 pN, to ensure a good fit. The obtained fit contact point was kept for the next analysis step, but the fitted Young's modulus was disregarded. In the second analysis step, the Hertz-Sneddon model was fitted again to corrected force-indentation curves, this time with a restriction to a 0.5 µm indentation depth, using the previously fitted contact point as a fixed parameter. The Young's modulus obtained in this second step was kept as the measured apparent Young's modulus of the corresponding indentation. Finally, the median Young's modulus across the 9 indentations was calculated for each cell. The values were pooled from three replicates and the comparison across knockdowns was plotted in Extended Data Fig. 8g.

The effective area modulus of nuclei across knockdowns was determined from individual AFM force-indentation curves in the presence of latrunculin A to remove cytoskeletal interference. The work done during indentation from 0 to 2 µm was calculated by integrating the area under the AFM force-indentation curve using trapezoidal method of numerical integration. The nuclear surface area change induced by indentation was quantified through 3D segmentation and surface fitting of volumetric images of nuclei acquired at 0 and 2 µm indentations, as previously described (Fig. 3b, Extended Data Fig. 8c). The effective area modulus (λ_{eff}) was then calculated using the following equation, incorporating the work done (*W*), the initial surface area at 0 µm indentation (*A*), and the area change upon indentation (*ΔA*):

$$\lambda_{eff} = \frac{2WA}{\Delta A^2}$$

The value of $\frac{A}{\Delta A^2}$ was calculated for six different cells as in Extended Data Fig. 8c and the mean of the values was used in the above equation.The histogram of λ_{eff} followed a lognormal distribution. The lognormal fit provided estimates for the mean, median, and mode of the distribution (Extended Data Fig. 8d,f). The calculated work done and λ_{eff} values were plotted as a scatter of individual points across conditions with mean ± s.d. (Fig. 3c,d Extended Data Fig. 8e).

Averaged force-indentation curves were obtained by aligning individual curves to the contact point using a custom Python script. Only curves that reached an

indentation of 2 μm were used. The mean ± s.d. of force at each indentation depth was then computed from the aligned curves and plotted in Extended Data Fig. 8a,b.

Statistical analysis and sample numbers

All experiments were repeated several times and indicated experiment numbers always refer to biological replicates for cell experiments and technical replicates for in-vitro experiments. Data were tested for normality or lognormality using Kolmogorov–Smirnov test. The appropriate statistical test was chosen as follows: Unpaired not normal distributed data containing only two groups: Mann-Whitney test, unpaired normal distributed data containing two or more groups: One-Way ANOVA with Tukey's test to correct for multiple comparisons and Unpaired not normal distributed data containing two or more groups: Kruskal Wallis test with multiple comparisons using Dunn's test. $\alpha = 0.05$ for all hypothesis testing.

References

1. Shah, P. *et al.* Nuclear Deformation Causes DNA Damage by Increasing Replication Stress. *Curr. Biol.* **31**, 753–765.e6 (2021).
2. Ganem, N. J. & Pellman, D. Linking abnormal mitosis to the acquisition of DNA damage. *J. Cell Biol.* **199**, 871–881 (2012).
3. Denais, C. M. *et al.* Nuclear envelope rupture and repair during cancer cell migration. *Science* (2016) doi:10.1126/science.aad7297.
4. Raab, M. *et al.* ESCRT III repairs nuclear envelope ruptures during cell migration to limit DNA damage and cell death. *Science* (2016) doi:10.1126/science.aad7611.
5. Ungricht, R. & Kutay, U. Mechanisms and functions of nuclear envelope remodelling. *Nature Reviews Molecular Cell Biology* vol. 18 229–245 Preprint at https://doi.org/10.1038/nrm.2016.153 (2017).
6. LaJoie, D. & Ullman, K. S. Coordinated events of nuclear assembly. *Current Opinion in Cell Biology* vol. 46 Preprint at https://doi.org/10.1016/j.ceb.2016.12.008 (2017).
7. von Appen, A. *et al.* LEM2 phase separation promotes ESCRT-mediated nuclear envelope reformation. *Nature* (2020) doi:10.1038/s41586-020-2232-x.
8. Gu, M. *et al.* LEM2 recruits CHMP7 for ESCRT-mediated nuclear envelope closure in fission yeast and human cells. *Proceedings of the National Academy of Sciences* **114**, E2166–E2175 (2017).
9. Samwer, M. *et al.* DNA Cross-Bridging Shapes a Single Nucleus from a Set of Mitotic Chromosomes. *Cell* (2017) doi:10.1016/j.cell.2017.07.038.

10. Skoko, D. *et al.* Barrier-to-autointegration factor (BAF) condenses DNA by looping. *Proceedings of the National Academy of Sciences* **106**, 16610–16615 (2009).
11. Liu, S. *et al.* Nuclear envelope assembly defects link mitotic errors to chromothripsis. *Nature* Preprint at https://doi.org/10.1038/s41586-018-0534-z (2018).
12. Ross, J. A. *et al.* Lem2 is essential for cardiac development by maintaining nuclear integrity. *Cardiovasc. Res.* **119**, 2074–2088 (2023).
13. Feurle, P. *et al.* SATB2‐LEMD2 interaction links nuclear shape plasticity to regulation of cognition‐related genes. *EMBO J.* (2021) doi:10.15252/embj.2019103701.
14. Nava, M. M. *et al.* Heterochromatin-Driven Nuclear Softening Protects the Genome against Mechanical Stress-Induced Damage. *Cell* **181**, 800–817.e22 (2020).
15. Papathanasiou, S. *et al.* Heritable transcriptional defects from aberrations of nuclear architecture. *Nature* **619**, 184–192 (2023).
16. Marbach, F. *et al.* The Discovery of a LEMD2-Associated Nuclear Envelopathy with Early Progeroid Appearance Suggests Advanced Applications for AI-Driven Facial Phenotyping. *Am. J. Hum. Genet.* (2019) doi:10.1016/j.ajhg.2019.02.021.
17. Caravia, X. M. *et al.* Loss of function of the nuclear envelope protein LEMD2 causes DNA damage-dependent cardiomyopathy. *J Clin Invest* **132**, (2022).
18. Barton, L. J., Soshnev, A. A. & Geyer, P. K. Networking in the nucleus: A spotlight on LEM-domain proteins. *Current Opinion in Cell Biology* Preprint at https://doi.org/10.1016/j.ceb.2015.03.005 (2015).
19. Tapia, O., Fong, L. G., Huber, M. D., Young, S. G. & Gerace, L. Nuclear envelope

protein Lem2 is required for mouse development and regulates MAP and AKT kinases. *PLoS One* (2015) doi:10.1371/journal.pone.0116196.

20. Schirmer, E. C., Florens, L., Guan, T., Yates, J. R., 3rd & Gerace, L. Nuclear membrane proteins with potential disease links found by subtractive proteomics. *Science* **301**, 1380–1382 (2003).
21. Ulbert, S., Antonin, W., Platani, M. & Mattaj, I. W. The inner nuclear membrane protein Lem2 is critical for normal nuclear envelope morphology. *FEBS Lett.* (2006) doi:10.1016/j.febslet.2006.10.060.
22. Halfmann, C. T. *et al.* Repair of nuclear ruptures requires barrier-to-autointegration factor. *J. Cell Biol.* **218**, 2136–2149 (2019).
23. Young, A. M., Gunn, A. L. & Hatch, E. M. BAF facilitates interphase nuclear membrane repair through recruitment of nuclear transmembrane proteins. *Mol. Biol. Cell* (2020) doi:10.1091/mbc.E20-01-0009.
24. Webster, B. M. *et al.* Chm7 and Heh1 collaborate to link nuclear pore complex quality control with nuclear envelope sealing. *EMBO J.* (2016) doi:10.15252/embj.201694574.
25. Brangwynne, C. P. *et al.* Germline P granules are liquid droplets that localize by controlled dissolution/condensation. *Science* (2009) doi:10.1126/science.1172046.
26. Li, P. *et al.* Phase transitions in the assembly of multivalent signalling proteins. *Nature* (2012) doi:10.1038/nature10879.
27. Frey, S., Richter, R. P. & Görlich, D. FG-rich repeats of nuclear pore proteins form a three-dimensional meshwork with hydrogel-like properties. *Science* (2006) doi:10.1126/science.1132516.

28. Kato, M. *et al.* Cell-free formation of RNA granules: low complexity sequence domains form dynamic fibers within hydrogels. *Cell* **149**, 753–767 (2012).
29. Quail, T. *et al.* Force generation by protein–DNA co-condensation. *Nat. Phys.* (2021) doi:10.1038/s41567-021-01285-1.
30. Renger, R. *et al.* Co-condensation of proteins with single- and double-stranded DNA. *Proc Natl Acad Sci U S A* **119**, e2107871119 (2022).
31. Keenen, M. M. *et al.* HP1 proteins compact DNA into mechanically and positionally stable phase separated domains. *Elife* **10**, (2021).
32. Zheng, R. *et al.* Barrier-to-autointegration factor (BAF) bridges DNA in a discrete, higher-order nucleoprotein complex. *Proc Natl Acad Sci U S A* **97**, 8997–9002 (2000).
33. Fritsch, A. W., Iglesias-Artola, J. M. & Hyman, A. A. inPhase - A simple, accurate and fast approach to determine phase diagrams of protein condensates. *bioRxiv* (2024) doi:10.1101/2024.10.02.616352.
34. Delcourt, S. G. & Blake, R. D. Stacking energies in DNA. *J Biol Chem* **266**, 15160–15169 (1991).
35. Cui, Y. & Bustamante, C. Pulling a single chromatin fiber reveals the forces that maintain its higher-order structure. *Proc Natl Acad Sci U S A* **97**, 127–132 (2000).
36. Mihardja, S., Spakowitz, A. J., Zhang, Y. & Bustamante, C. Effect of force on mononucleosomal dynamics. *Proc Natl Acad Sci U S A* **103**, 15871–15876 (2006).
37. van Mameren, J. *et al.* Unraveling the structure of DNA during overstretching by using multicolor, single-molecule fluorescence imaging. *Proceedings of the National Academy of Sciences* **106**, 18231–18236 (2009).

38. Jülicher, F. & Weber, C. A. Droplet Physics and Intracellular Phase Separation. *Annu. Rev. Condens. Matter Phys.* **15**, 237–261 (2024).

39. King, G. A., Biebricher, A. S., Heller, I., Peterman, E. J. G. & Wuite, G. J. L. Quantifying local molecular tension using intercalated DNA fluorescence. *Nano Lett.* **18**, 2274–2281 (2018).

40. Ozdilek, B. A. *et al.* Intrinsically disordered RGG/RG domains mediate degenerate specificity in RNA binding. *Nucleic Acids Res* **45**, 7984–7996 (2017).

41. Jung-Garcia, Y. *et al.* LAP1 supports nuclear adaptability during constrained melanoma cell migration and invasion. *Nat Cell Biol* **25**, 108–119 (2023).

42. Vietri, M. *et al.* Unrestrained ESCRT-III drives micronuclear catastrophe and chromosome fragmentation. *Nat. Cell Biol.* (2020) doi:10.1038/s41556-020-0537-5.

43. Taniguchi, R. *et al.* Nuclear pores safeguard the integrity of the nuclear envelope. *bioRxiv* (2024) doi:10.1101/2024.02.05.578890.

44. Turgay, Y. *et al.* The molecular architecture of lamins in somatic cells. *Nature* (2017) doi:10.1038/nature21382.

45. Mahamid, J. *et al.* Visualizing the molecular sociology at the HeLa cell nuclear periphery. *Science* (2016) doi:10.1126/science.aad8857.

46. Horikoshi, N. *et al.* Cryo-EM structures of the BAF-Lamin A/C complex bound to nucleosomes. *Nat Commun* **16**, 1495 (2025).

47. Samson, C. *et al.* Structural analysis of the ternary complex between lamin A/C, BAF and emerin identifies an interface disrupted in autosomal recessive progeroid diseases. *Nucleic Acids Res.* **46**, 10460–10473 (2018).

48. Brachner, A. LEM2 is a novel MAN1-related inner nuclear membrane protein

associated with A-type lamins. *J. Cell Sci.* (2005) doi:10.1242/jcs.02701.

49. Mostafazadeh, N. & Peng, Z. Microstructure-based nuclear lamina constitutive model. *Cytoskeleton (Hoboken)* **81**, 297–309 (2024).
50. Liu, C. *et al.* Tough hydrogels with rapid self-reinforcement. *Science* **372**, 1078–1081 (2021).
51. Petelinšek, N. & Mommer, S. Tough Hydrogels for Load-Bearing Applications. *Adv Sci (Weinh)* **11**, e2307404 (2024).
52. Solovei, I. *et al.* LBR and lamin A/C sequentially tether peripheral heterochromatin and inversely regulate differentiation. *Cell* **152**, 584–598 (2013).
53. Dahl, K. N., Kahn, S. M., Wilson, K. L. & Discher, D. E. The nuclear envelope lamina network has elasticity and a compressibility limit suggestive of a molecular shock absorber. *J. Cell Sci.* **117**, 4779–4786 (2004).
54. Swift, J. *et al.* Nuclear Lamin-A Scales with Tissue Stiffness and Enhances Matrix-Directed Differentiation. *Science* **341**, 1240104 (2013).
55. Sanulli, S. *et al.* HP1 reshapes nucleosome core to promote phase separation of heterochromatin. *Nature* **575**, 390–394 (2019).
56. Zhang, M. *et al.* Lamin A/C safeguards replication initiation by orchestrating chromatin accessibility and PCNA recruitment. *bioRxivorg* 2025.03.06.641818 (2025).
57. Cherdyntseva, V. *et al.* Nucleoplasmic Lamin A/C controls replication fork restart upon stress by modulating local H3K9me3 and ADP-ribosylation levels. *bioRxivorg* 2025.01.18.633737 (2025).
58. Sidorenko, E. *et al.* Lamina-associated polypeptide 2α is required for intranuclear

MRTF-A activity. *Sci Rep* **12**, 2306 (2022).

59. Ferraioli, S. *et al.* LAP2alpha facilitates myogenic gene expression by preventing nucleoplasmic lamin A/C from spreading to active chromatin regions. *Nucleic Acids Res* **52**, 11500–11518 (2024).
60. Cai, M. *et al.* Solution NMR structure of the barrier-to-autointegration factor-emerin complex. *J. Biol. Chem.* (2007) doi:10.1074/jbc.M700576200.
61. Bradley, C. M., Ronning, D. R., Ghirlando, R., Craigie, R. & Dyda, F. Structural basis for DNA bridging by barrier-to-autointegration factor. *Nat. Struct. Mol. Biol.* **12**, 935–936 (2005).
62. Jumper, J. *et al.* Highly accurate protein structure prediction with AlphaFold. *Nature* **596**, 583–589 (2021).
63. Pettersen, E. F. *et al.* UCSF ChimeraX: Structure visualization for researchers, educators, and developers. *Protein Sci.* **30**, 70–82 (2021).
64. Cho, N. H. *et al.* OpenCell: Endogenous tagging for the cartography of human cellular organization. *Science* **375**, eabi6983 (2022).
65. Spakman, D., King, G. A., Peterman, E. J. G. & Wuite, G. J. L. Constructing arrays of nucleosome positioning sequences using Gibson Assembly for single-molecule studies. *Sci Rep* **10**, 9903 (2020).
66. Aicart-Ramos, C., Hormeno, S., Wilkinson, O. J., Dillingham, M. S. & Moreno-Herrero, F. Long DNA constructs to study helicases and nucleic acid translocases using optical tweezers. *Methods Enzymol* **673**, 311–358 (2022).
67. Liu, Y.-T. *et al.* Isotropic reconstruction for electron tomography with deep learning. *Nat. Commun.* **13**, 6482 (2022).

68. Heebner, J. E. *et al.* Deep Learning-Based Segmentation of Cryo-Electron Tomograms. *J Vis Exp* (2022) doi:10.3791/64435.

69. Kremer, J. R., Mastronarde, D. N. & Mcintosh, J. R. Computer visualization of three-dimensional image data using IMOD J. *J. Struct. Biol* **116**, 71–76 (1996).